

Tunable creation of pure spin supercurrents via Rashba spin-orbit coupling with Pt/Co/Pt spin sinks

Kun-Rok Jeon,^{1,2*} Xavier Montiel,³ Chiara Ciccarelli,² Hidekazu Kurebayashi,⁴
Lesley F. Cohen,⁵ Sachio Komori,¹ Mark G. Blamire¹ and Jason W. A. Robinson^{1*}

¹*Department of Materials Science and Metallurgy, University of Cambridge, 27 Charles
Babbage Road, Cambridge CB3 0FS, United Kingdom*

²*Cavendish Laboratory, University of Cambridge, Cambridge CB3 0HE, United
Kingdom*

³*Department of Physics, Royal Holloway, University of London, Egham Hill, Egham,
Surrey TW20 0EX, United Kingdom*

⁴*London Centre for Nanotechnology and Department of Electronic and Electrical
Engineering at University of College London, London WC1H 0IH, United Kingdom*

⁵*The Blackett Laboratory, Imperial College London, SW7 2AZ, United Kingdom*

*To whom correspondence should be addressed: jeonkunrok@gmail.com,

jjr33@cam.ac.uk

Superconducting spin currents are key to the development of superconducting spintronics and involve the transfer of spin angular momentum via proximity-induced equal-spin triplet states in a singlet superconductor (SC)¹⁻³. Recently developed theory⁴⁻⁸ and experimental results⁹⁻¹³ show that spin-orbit coupling (SOC) in conjunction with a magnetic exchange field h_{ex} generates spin-polarized triplet pairs. Here we demonstrate that when a perpendicularly magnetized Pt/Co/Pt spin sink is proximity-coupled to Nb (a singlet SC), spin-pumping efficiency in the superconducting state is tunable by controlling the tilt angle θ_{Co} of the Co layer magnetization, thus increasing the degree of orthogonality between the SOC and h_{ex}

at the Nb/Pt/(Co/Pt) interface^{4-6,8}. We also disentangle the contribution of interfacial SOC to the θ_{Co} -dependent superconducting spin-pumping efficiency from other contributions by inserting a thin Cu spacer with weak SOC at the Nb/Pt/(Co/Pt) interface and find a sinusoidal maximum at $\theta_{Co} \approx 45^\circ$, reflecting the characteristic features of Rashba SOC-induced triplet pairing^{4-6,8}.

Spin-triplet Cooper pairs carry a net spin component in addition to charge and are therefore key to the development of superconducting spintronics¹⁻³, underlying a future revolution in energy-efficient computing. It is established that spin-polarized triplet pairs are generated via spin-mixing and spin-rotation processes at magnetically-inhomogeneous SC/ferromagnet (FM) interfaces¹⁻³. Recently, theoretical⁴⁻⁸ and experimental studies⁹⁻¹³ have been dedicated to an alternative mechanism for triplet pair creation involving SOC in combination with h_{ex} . In such systems, triplet pair creation depends on the commutation relationship⁴⁻⁷ between SOC and h_{ex} .

The latter mechanism via SOC in conjunction with h_{ex} offers a conceptually novel approach to tune superconducting spin currents, as we demonstrate here using ferromagnetic resonance (FMR) spin pumping^{9,14}. When a perpendicularly magnetized Pt/Co/Pt spin-sink is proximity-coupled to Nb (singlet SC) (Fig. 1a), the t_{Co} -dependent magnetization anisotropy^{15,16} changes the effective θ_{Co} under in-plane (IP) FMR condition of the IP magnetized Ni_8Fe_2 (Fig. 1b) and in turn alters the degree of orthogonality between h_{ex} and SOC at the Nb/Pt/(Co/Pt) interface. Manipulating θ_{Co} determines the efficiency in which spin-zero triplets (converted from spin singlets by the presence of h_{ex}) rotate to form equal-spin triplets⁴⁻⁶. This enables orthogonality tuning of spin-angular-momentum transfer from the precessing Ni_8Fe_2 through the proximity-

induced equal-spin triplets into singlet Nb layers, which we call superconducting pure spin currents⁹. The enhanced spin pumping/transfer is probed by measuring the FMR linewidth broadening or Gilbert damping increase of the middle Ni₈Fe₂ layer^{9,14}.

To demonstrate our approach, we perform a series of FMR measurements on Pt/Co/Pt/Nb/Ni₈Fe₂/Nb/Pt/Co/Pt multilayers (Fig. 1a). The ultrathin (≤ 1.5 nm) perpendicularly magnetized Co layers serve as an internal source of h_{ex} to the neighbouring (inner) Pt layers, supplying spontaneous spin splitting^{17,18} with out-of-plane (OOP) polarization (Fig. 1a); the outer Pt layers boost the perpendicular anisotropy of the Co as well as the total effective spin conductance of Pt/Co/Pt trilayers¹⁹. By inserting a thin Cu spacer with weak SOC at the interface between Nb and Pt/(Co/Pt) layers (Fig. 1a), we are able to separate the contribution of interfacial Rashba-type SOC to the θ_{Co} -dependent superconducting spin-pumping efficiency from other contributions and to compare it with the prediction from spin-triplet proximity theory^{4-6,8}.

We first measure the t_{Co} -dependence of the superconducting transition T_c (Fig. 1c) for a series of multilayers with and without Cu spacers. T_c decreases rapidly with increasing t_{Co} until it reaches about 1.5 nm where it slightly increases. No significant change in $T_c(t_{\text{Co}})$ appears with the addition of the Cu spacer, consistent with its long superconducting coherence length of several hundred nanometers³. Such non-monotonic T_c behaviour has been previously discussed^{20,21} based on a spatial modulation of the superconducting order parameter due to Cooper pairs acquiring a non-zero net momentum in the presence of h_{ex} ; in particular, for SC/FM multilayers or SC/FM bilayers with FM thickness t_{FM} of the order of the coherence length ξ_{FM} , which leads to a damped oscillatory behaviour of the order parameter^{20,21}. A quantitative analysis (see Methods) of the T_c data (black lines, Fig. 1c) gives an effective ξ_{FM} of 1.4–1.6 nm and interface

transparency $\gamma_B = 0.18\text{--}0.20$ for our samples, which are in reasonable agreement with those obtained from Nb/FM²² bilayers and Nb/Cu/FM trilayers²³ with strong FMs.

The t_{Co} -dependent magnetization anisotropy of the Pt/Co/Pt spin sinks can be independently characterized by static magnetometry measurements on Pt/Co/Pt/Nb-only films with different t_{Co} . Figure 1d shows the typical magnetization $M(H)$ curves obtained at 8 K by applying the external magnetic field $\mu_0 H$ parallel and perpendicular to the film plane. At low t_{Co} (≤ 0.8 nm), the easy axis of the Co magnetization M_{Co} is clearly OOP, indicating that the ultrathin Co sandwiched between two Pt layers has well-established perpendicular magnetization anisotropy (PMA), as expected for the Pt 5d–Co 3d orbital hybridization at either Pt/Co interface plus SOC¹⁸. As t_{Co} approaches 1.5 nm, the predominant magnetization anisotropy changes from OOP to IP, exhibiting the reorientation transition¹⁶. Using the relationship¹⁶ $\mu_0 H_{\text{ani}} \cdot M_s / 2 = K_{\text{eff}}$, where $\mu_0 H_{\text{ani}}$ is the anisotropy field and M_s is the saturation magnetization, the effective PMA energy K_{eff} is estimated for $t_{\text{Co}} \leq 0.8$ nm to be ~ 1 MJ m⁻³, comparable to typical values of the perpendicularly magnetized Pt/Co/Pt trilayers²⁴.

Assuming coherent rotation of M_{Co} from OOP under the application of IP resonance fields $\mu_0 H_{\text{res}}$ for the middle Ni₈Fe₂, the effective θ_{Co} can be estimate using the simplified Stoner-Wohlfarth model where $\theta_{\text{Co}} = \arccos[M(\mu_0 H_{\text{res}})/M_s]$. We then achieve discrete tilt states of the Pt/Co/Pt spin sinks from OOP to IP (Fig. 1e), which are systematically controllable by varying t_{Co} .

We next show the influence of the tilt states on the superconducting spin-pumping efficiency, namely that the associated orthogonality between h_{ex} and SOC at the Nb/Pt/(Co/Pt) interface strongly modifies the spin-angular-momentum transfer in the superconducting state. Figure 2a,b shows the microwave frequency f dependence of FMR

data for the Cu-absent (Cu-present) samples, taken above and below T_c of the Nb layers. From this, we extract the effective Gilbert damping α , which provides a measure^{9,14,18} of the net spin current flow out of the precessing Ni_3Fe_2 , and the effective saturation magnetization $\mu_0 M_s$ (see Methods).

The extracted α and $\mu_0 M_s$ values are plotted as a function of t_{Co} in Fig. 2c. In the normal state ($T/T_c > 1$), α is almost t_{Co} -independent for both sample sets and there is a small decrease in the magnitude by introducing Cu spacers. This means that the presence of ultrathin Co (≤ 2 nm) and Cu (5 nm) layers hardly changes the normal-state spin-pumping behaviour, as expected from their small spin conductances¹⁹ relative to Pt and the three layers (Co, Cu, Pt) are all approximately spin-transparent²⁵ with each other due to their similar crystal and electronic structures.

However, in the superconducting state ($T/T_c < 1$), a significant t_{Co} -dependent enhancement of α appears and is strongly affected by the addition of Cu. For the Cu-absent multilayers, as t_{Co} increases the superconducting-state damping enhancement (indicating the enhanced spin flow/transfer mediated most likely by equal-spin triplet pairing)^{8,14,18} rapidly rises until reaching 0.8 nm and then slowly decreases for thicker Co layers, resulting in a maximum at $t_{\text{Co}} \approx 0.8$ nm. For the Cu-present samples, the overall amplitude of damping enhancement diminishes compared with the Cu-absent samples and the maximum moves to a lower value of t_{Co} (0.4 nm). Since this non-trivial enhancement of $\alpha(t_{\text{Co}})$ occurs in the ultrathin regime ($t_{\text{Co}} \leq 2$ nm, about one order of magnitude smaller than the spin diffusion length²⁶) only for the superconducting state, it must reflect how the tilt states of the Pt/Co/Pt spin sinks correlate with the superconducting spin transport.

To elucidate this, we plot the damping difference across T_c , defined as $[\alpha_{2\text{K}} - \alpha_8$

$\kappa]/2\Delta_{2\text{ K}}$ where 2Δ is the superconducting gap at 2 K calculated from the measured T_c (Fig. 1d), with and without Cu spacers as a function of the effective θ_{Co} (Fig. 2e). In the absence of the Cu spacers, $[\alpha_{2\text{ K}} - \alpha_{8\text{ K}}]/2\Delta_{2\text{ K}}$ rapidly rises with increasing θ_{Co} from 0° to 56° followed a fall for a higher angle. However, this characteristic angular dependence vanishes when the Cu spacer (with weak SOC) is present: the damping difference increases monotonically/slowly up to the highest angle and it saturates to the similar value of the Cu-absent $\theta_{\text{Co}} \approx 76^\circ$ ($t_{\text{Co}} = 0.4\text{ nm}$) sample.

There are, in principle, two different sources of proximity-induced triplet pairing which can contribute to the characteristic angular dependence observed in our experimental setup. Firstly, it is well-known that magnetization noncollinearity (or inhomogeneity)^{1-3,27} between two FMs separated by a SC of the order of the coherence length can generate equal-spin triplets through the entire structure. The equal-spin triplet density is then ascribed to the relative magnetization angle θ between the two FMs²⁷: $\propto \mathbf{M}_1 \times \mathbf{M}_2 \propto \sin(\theta)$. This explains why our $\theta_{\text{Co}} \approx 76^\circ$ ($t_{\text{Co}} = 0.4\text{ nm}$) samples reveal larger enhancements than $\theta_{\text{Co}} \approx 9^\circ$ ($t_{\text{Co}} = 2.0\text{ nm}$) samples (Fig. 2e). Secondly, even for a single magnetically-homogeneous FM, the equal-spin triplet correlation can be generated by introducing a strongly SO coupled interface (e.g. Pt) between the FM and SC^{4-6,8}. In this case, the singlet-triplet conversion efficiency is predicted to scale with the degree of orthogonality between SOC and h_{ex} ; or equivalently, the cross product of the SO vector operator $[\hat{A}_k, [\hat{A}_k, h^a \sigma^a]]$ and the exchange field operator $h^a \sigma^a$. Here $\hat{A}_{k=x,y,z}$ is the vector potential describing the form of the SOC, for instance, the Rashba constant α_R (Dresselhaus constant β_D) due to the interface (bulk) inversion asymmetry. σ^a (h^a) with $a = x,y,z$ is the vector of Pauli (exchange field) matrices.

For a metallic vertical structure with *atomically flat* interfaces, the vector potential

can be approximated as^{4,5}: $\hat{A}_x \approx 0$, $\hat{A}_y \approx -\beta_D \sigma^y + \alpha_R \sigma^z$, $\hat{A}_z \approx \beta_D \sigma^z - \alpha_R \sigma^y$. With finite Rashba ($\alpha_R \neq 0$) and zero Dresselhaus ($\beta_D = 0$) contribution to the SOC^{6,8}, as relevant to our experimental setup, a sinusoidal maximum of the equal-spin triplet correlation is expected when the canting angle between IP and OOP components of h_{ex} becomes 45° . In such a case, the overall triplet density is quadratic in α_R and so very sensitive to details of the spin-orbit coupled interface. The addition of a-few-nm-thick Cu spacer layers^{25,28} at the spin-orbit coupled interface turns out to be sufficient to significantly quench the interfacial Rashba-type SOC, thus providing an important test experiment for the responsible mechanism, being done clearly here (inset of Fig. 2e,f). We also note that non-vanishing of $\hat{A}_x (\neq 0)$, as would be expected from *non-ideal* interfaces where OOP component of the Rashba SO field with respect to the local interface plane survives on a scale of the coherence length⁷, allows the equal-spin triplet to be generated even with a purely IP magnetized FM ($h^x = 0$). This is a likely mechanism for our previous FMR experiments^{9,18} and for the $t_{\text{Co}} = 0$ samples (Fig. 2e).

By taking all these effects together, we can arrive at good fits to $[\alpha_{2\text{K}} - \alpha_{8\text{K}}]/2\Delta_{2\text{K}}$ vs. θ_{Co} data for both sample sets (black solid and dashed lines in Fig. 2e, see Supplementary Section 1,2), thereby reproducing the experimental results and capturing the underlying physics. To focus on the second SOC mechanism, in particular for the interfacial contribution, we take the difference between the data with and without the Cu spacer (Fig. 2f). We then find an approximately sinusoidal maximum at $\theta_{\text{Co}} \approx 45^\circ$, which is in good agreement with the Rashba SOC-induced triplet pairing^{6,8} described above. The data described above provides a proof-of-concept result demonstrating the orthogonality tuning of superconducting spin currents.

To help understand better the FMR absorption data of symmetric structures (Fig.

2), we also measure the t_{Co} -dependence of spin-pumping-induced inverse spin-Hall effect (iSHE)^{29,30} for the additional sets of asymmetric Pt/Co/Pt/Nb/Ni₈Fe₂ structures with and without Cu spacers. This provides direct evidence for spin transport in the normal state. Figure 3a (3b) displays the transverse d.c. voltage signals vs. external IP $\mu_0 H$ for the Cu-absent (Cu-present) samples at $f = 5$ GHz, taken above and below T_c (see Methods). Under IP FMR of the Ni₈Fe₂, a clear Lorentzian peak emerges in the dc voltage only in the normal state for both sample sets, which can be explained³⁰ by the strongly suppressed quasiparticle charge imbalance effect across T_c . Importantly, the polarity of the Lorentzian peak is identical (opposite) to that of Pt/Ni₈Fe₂ (Nb/Ni₈Fe₂) bilayers³⁰, where the Pt (Nb) spin sink is known to have a positive (negative) spin-Hall angle θ_{SH} ^{19,30}. This indicates that the pumped spin currents from the precessing Ni₈Fe₂ pass through the Nb(30 nm) layer to a large extent to the (Cu)/Pt/Co/Pt spin sinks and the overall iSHE in our structures is dominated by the (Cu)/Pt/Co/Pt (rather than the Nb).

For a quantitative analysis, we plot the iSHE voltage divided by sample resistance V_{iSHE}/R vs. t_{Co} (Fig. 3c) and θ_{Co} (Fig. 3d). In these plots, we can see that there is a clear decrease in the iSHE signal by the addition of Cu and its magnitude is strongly θ_{Co} -dependent, which can be described by the rapid spin precession/dephasing of transverse spins³¹ around h_{ex} of the Co layer: $\cos^2(\theta_{\text{Co}})$ (black lines in Fig. 3d). Note that the signal difference caused by the addition of 5 nm of Cu (insets in Fig. 3c,d) is nearly θ_{Co} -independent. These results taken together support our argument that Cu spacers weaken the interfacial SOC strength and it is the Co tilt state that then plays a dominant role in the spin transport process.

We have shown that when a perpendicularly magnetized Pt/Co/Pt spin sink is proximity-coupled to Nb, superconducting spin-pumping efficiency can be tuned by

controlling the effective θ_{Co} - i.e. by tuning the degree of orthogonality between the SOC and h_{ex} at the Nb/Pt/(Co/Pt) interface^{4-6,8}. We have also found that by comparison with the Cu-present samples, the θ_{Co} -dependent superconducting spin-pumping efficiency reflects characteristic features of Rashba SOC-induced triplet pairing^{4-6,8}. Our results provide a timely step towards understanding key interfacial properties for tuning superconducting spin transport mediated via equal-spin triplet states in a spin-singlet superconductor. This concept can be extended to any Rashba system³² for the development of superconducting spin-logic devices¹ in which SOC is gate-tunable³², leading to a superconducting spin-based transistor.

Methods

Methods and any associated references are available in the online version of the paper.

References

1. Linder, J. & Robinson, J. W. A. Superconducting spintronics. *Nat. Phys.* **11**, 307–315 (2015).
2. Eschrig, M. Spin-polarized supercurrents for spintronics: a review of current progress. *Rep. Prog. Phys.* **78**, 104501 (2015).
3. Birge, N. O. Spin-triplet supercurrents in Josephson junctions containing strong ferromagnetic materials. *Phil. Trans. R. Soc. A* **376**, 20150150 (2018).
4. Bergeret, F. S. & Tokatly, I. V. Spin-orbit coupling as a source of long-range triplet proximity effect in superconductor-ferromagnet hybrid structures. *Phys. Rev. B* **89**, 134517 (2014).
5. Jacobsen, Sol H., Ouassou, Jabir A. & Linder, J. Critical temperature and tunneling spectroscopy of superconductor-ferromagnet hybrids with intrinsic Rashba-Dresselhaus

- spin-orbit coupling. *Phys. Rev. B* **92**, 024510 (2015).
6. Jacobsen, Sol H., Kulagina, I. & Linder, J. Controlling superconducting spin flow with spin-flip immunity using a single homogeneous ferromagnet. *Sci. Rep.* **6**, 23926 (2016).
 7. Montiel, X. & Eschrig, M. Generation of pure superconducting spin current in magnetic heterostructures via nonlocally induced magnetism due to Landau Fermi liquid effects. *Phys. Rev. B* **98**, 104513 (2018).
 8. Amundsen, M. & Linder, J. The quasiclassical theory for interfaces with spin-orbit coupling. arXiv:1904.11986 (2019).
 9. Jeon, K.-R. et al. Enhanced spin pumping into superconductors provides evidence for superconducting pure spin currents. *Nat. Mater.* **17**, 499–503 (2018).
 10. Banerjee, N., Ouassou, J. A., Zhu, Y., Stelmashenko, N. A., Linder, J. & Blamire, M. G. Controlling the superconducting transition by spin-orbit coupling. *Phys. Rev. B* **97**, 184521 (2018).
 11. Satchell, N. & Birge, N. O. Supercurrent in ferromagnetic Josephson junctions with heavy metal interlayers. *Phys. Rev. B* **97**, 214509 (2018).
 12. Satchell, N., Loloee, R. & Birge, N. O. Supercurrent in ferromagnetic Josephson junctions with heavy metal interlayers II: canted magnetization. arXiv:1904.08798 (2019).
 13. Martínez, I. et al. Interfacial Spin-Orbit Coupling: New Platform for Superconducting Spintronics, arXiv:1812.08090 (2018).
 14. Tserkovnyak, Y., Brataas, A., Bauer, G. E. W. & Halperin, B. I. Nonlocal magnetization dynamics in ferromagnetic heterostructures. *Rev. Mod. Phys.* **77**, 1375–1421 (2005).
 15. Nakajima, N. et al. Perpendicular Magnetic Anisotropy Caused by Interfacial

Hybridization via Enhanced Orbital Moment in Co/Pt Multilayers: Magnetic Circular X-Ray Dichroism Study. *Phys. Rev. Lett.* **81**, 5229-5232 (1998).

16. Johnson, M. T., Bloemen, P. J. H., a Den Broeder, F. J. and De Vries, J. J. Magnetic anisotropy in metallic multilayers. *Reports Prog. Phys.* **59**, 1409-1458 (1999).

17. Klewe, C. et al. Static magnetic proximity effect in Pt/Ni_{1-x}Fe_x bilayers investigated by x-ray resonant magnetic reflectivity. *Phys. Rev. B* **93**, 214440 (2016).

18. Jeon, K.-R. et al. Exchange-field enhancement of superconducting spin pumping. *Phys. Rev. B* **99**, 024507 (2019).

19. Tanaka, T., Kontani, H., Naito, M., Naito, T., Hirashima, D. S., Yamada, K. & Inoue, J. Intrinsic spin Hall effect and orbital Hall effect in 4d and 5d transition metals. *Phys. Rev. B* **77**, 165117 (2008).

20. Larkin, A. I. & Ovchinnikov, Y. N. Nonuniform state of superconductors. *Zh. Eksp. Teor. Fiz.* **47**, 1136-1146 (1964); *Sov. Phys. JETP* **20**, 762-769 (1965).

21. Buzdin, A. I. Proximity effects in superconductor-ferromagnet heterostructures. *Rev. Mod. Phys.* **77**, 935-975 (2005).

22. Kim, J., Kwon, J. H., Char, K., Doh, H. & Choi, H.-Y. Quantitative analysis of the proximity effect in Nb/Co₆₀Fe₄₀, Nb/Ni, and Nb/Cu₄₀Ni₆₀ bilayers. *Phys. Rev. B* **72**, 014518 (2005).

23. Kim, K., Kwon, J. H., Kim, J., Char, K., Doh, H. & Choi, H.-Y. Proximity effect in Nb/Cu/CoFe trilayers. *Phys. Rev. B* **74**, 174503 (2006).

24. Lee, T. Y., Won, Y. C., Son, D. S., Lim, S. H. & Lee, S.-R. Strength of Perpendicular Magnetic Anisotropy at Bottom and Top Interfaces in [Pt/Co/Pt] Trilayers. *IEEE Mag. Lett.* **5**, 1000104 (2014).

25. Zhang, W., Han, W., Jiang, X., Yang, S.-H. & Parkin, S. S. P. Role of transparency

of platinum–ferromagnet interfaces in determining the intrinsic magnitude of the spin Hall effect. *Nat. Phys.* **11**, 496–502 (2015).

26. Bass, J. & P Pratt Jr, W. Spin-diffusion lengths in metals and alloys, and spin-flipping at metal/metal interfaces: an experimentalist's critical review. *J. Phys.: Condens. Matter* **19**, 183201 (2007).

27. Fominova, Ya. V., Golubovb, A. A., Karminskayac, T. Yu., Kupriyanovc, M. Yu., Deminovd, R. G. and Tagirovd L. R. Superconducting Triplet Spin Valve. *JETP Lett.* **91**, 308-313 (2010).

28. Zhou, L. et al. Observation of spin-orbit magnetoresistance in metallic thin films on magnetic insulators. *Sci. Adv.* **4**, eaao3318 (2018).

29. Saitoh, E., Ueda, M., Miyajima, H. & Tatara, G. Conversion of spin current into charge current at room temperature: Inverse spin-Hall effect. *Appl. Phys. Lett.* **88**, 182509 (2006).

30. Jeon, K.-R. et al. Spin-pumping-induced inverse spin-Hall effect in Nb/Ni₈₀Fe₂₀ bilayers and its strong decay across the superconducting transition temperature. *Phys. Rev. Applied* **10**, 014029 (2018).

31. Brataas, A., Kent, A. D. & Ohno, H. Current-induced torques in magnetic materials. *Nat. Mater.* **11**, 372 (2012).

32. Manchon. A., Koo. H. C., Nitta, J., Frolov, S. M. & Duine, R. A. New perspectives for Rashba spin–orbit coupling, *Nat. Mater.* **14**, 871 (2015).

Acknowledgements

This work was supported by EPSRC Programme Grant EP/N017242/1.

Author contributions

K.-R.J. and J.W.A.R. conceived and designed the experiments. The samples were prepared by K.-R.J. and the magnetization and transport measurements were performed by K.-R.J. with help from S.K. The FMR absorption and iSHE measurements were carried out by K.-R.J. with help of C.C. The data analysis was performed by K.-R.J., C.C., H.K., L.F.C., M.G.B., S.K. and J.W.A.R. The model calculation was undertaken by X.M. All authors discussed the results and commented on the manuscript, which was written by K.-R., X.M. and J.W.A.R.

Additional information

Supplementary information is available for this paper here (TBD). Reprints and permissions information is available at www.nature.com/reprints. Correspondence and requests for materials should be addressed to K.-R.J. or J.W.A.R.

Competing interests

The authors declare no competing financial interests.

Methods

Sample growth. Symmetric Pt/Co/Pt/Nb/Ni₈Fe₂/Nb/Pt/Co/Pt and asymmetric Pt/Co/Pt/Nb/Ni₈Fe₂ multilayers, with and without Cu spacer layers, were grown on 5 mm × 5 mm thermally oxidized Si substrates by d.c. magnetron sputtering in an ultra-high vacuum chamber^{9,18}. The symmetric and asymmetric structures were prepared, respectively, for the ferromagnetic resonance (FMR) absorption^{9,18} and inverse spin-Hall effect (iSHE, or transverse d.c. voltage)³⁰ measurements. All layers were grown *in-situ* at

room temperature. Ni_8Fe_2 , Nb, Co and Cu are deposited at an Ar pressure of 1.5 Pa and Pt at 3.0 Pa. The typical deposition rates were 5.1 nm/min for Ni_8Fe_2 , 21.1 nm/min for Nb, 6.0 nm/min for Co, 9.7 nm/min for Cu and 7.6 nm/min for Pt. The thicknesses of Ni_8Fe_2 , Nb, inner (outer) Pt and Cu layers were kept constant at 6, 30, 1.7 (2.2) and 5 nm, respectively, while the thickness of the Co layer varied from 0 to 2 nm to investigate the variation of FMR damping as a function of t_{Co} (or the Co tilt angle θ_{Co}) through the superconducting transition temperature T_c of the coupled Nb. Note that for all samples, the Nb (inner Pt) thickness is fixed at 30 (1.7) nm where the Pt/Co/Pt spin sink was proximity-coupled through the Nb layer to the precessing Ni_8Fe_2 layer and the largest enhancement of spin pumping in the superconducting state was achieved in our prior FMR experiments^{9,18}.

Magnetization characterization. The static magnetization curves were measured on 5 mm \times 5 mm samples using a Quantum Design Magnetic Property Measurement System at 8 K, immediately above the superconducting transition temperature T_c . The external magnetic field was applied parallel and perpendicular to the film plane direction.

Superconducting transition measurement. d.c. electrical transport measurements were conducted on (un-patterned) 5 mm \times 5 mm samples using a custom-built dipstick probe in a liquid helium dewar with a four-point current-voltage method. The resistance R (of a sample) vs. temperature T curves were obtained at the applied current I of ≤ 0.1 mA while decreasing T . From the T derivative of R , dR/dT , T_c was defined as the T value that exhibits the maximum of dR/dT .

We analyzed our $T_c(t_{\text{Co}})$ data (Fig. 1d) using the following approximate formula²¹:

$$\ln \left[\frac{T_c^*}{T_c} \right] \approx \Psi \left(\frac{1}{2} \right) - \text{Re} \left\{ \Psi \left[\frac{1}{2} + \frac{2T_c}{T_c^* \tilde{\tau}_0} \times \frac{1}{\tilde{\gamma} + \frac{1-i}{2} \cosh[(1+i)t_{FM}]} \right] \right\}, \text{ where } T_c^* = T_c(t_{FM} = 0), \Psi$$

is the digamma function, $\tilde{\tau}_0^{-1} = (1/4\pi T_c)(D_{SC}/t_{SC}\xi_{FM})(\rho_{SC}/\rho_{FM})$, D_{SC} is the diffusion coefficient of the Nb (10 cm²/s at 8 K), t_{SC} is the Nb thickness (30 nm) and ρ_{SC} (ρ_{FM}) is the conductivity of the Nb (Co) [7 (30) $\mu\Omega\text{-cm}$ at 8 K]. $\tilde{\gamma} = \gamma_B(\xi_{SC}/\xi_{FM})$, γ_B is the interface transparency and ξ_{SC} is the (dirty-limit) coherence length of the Nb (16–18 nm at 2 K)⁹. Note that in this formula, only the influence of h_{ex} on the order parameter is taken into account^{20,21}.

Broadband FMR absorption and iSHE measurements. We measured the FMR response of the sample attached on a broadband coplanar waveguide (CPW) with either d.c. field or r.f. pulse modulation^{9,18}. To obtain each FMR spectrum, the microwave power absorbed by the sample was measured while sweeping the external static magnetic field $\mu_0 H$ at the fixed microwave frequency f of 5–20 GHz. At the beginning of each measurement, we applied a large IP $\mu_0 H$ (0.5 T) to fully magnetize the Ni₈Fe₂ layer, after which the field was reduced to the range of FMR. Once the f -dependent FMR measurements (from high to low f) were complete, the field was returned to zero to cool the system down further for a lower T measurement. For all FMR absorption measurements, the microwave power was set to 10 dBm where the actual microwave power absorbed in the sample is a few mW that has no effect on T_c of the Nb layer⁹. Note also that the fixed thickness (30 nm) of Nb layers studied here is much less than the magnetic penetration depth in the superconducting state (≥ 100 nm in thin Nb films) and so there is no considerable effect of Meissner screening on the local (d.c./r.f.) magnetic field experienced by Ni₈Fe₂ below T_c , as supported by the insensitivity of the resonance field $\mu_0 H_{res}$ across T_c (Fig. 2a,b). We employed a vector field cryostat from Cryogenic

Ltd. that can apply a 1.2-T-magnetic field in any direction over a T range of 2–300 K.

We first fitted the FMR absorption data (Supplementary Section 3) with the field derivative of symmetric and antisymmetric Lorentzian functions³³ to accurately determine the FMR linewidth $\mu_0\Delta H$ and the resonance field μ_0H_{res} : $\frac{d\chi''}{dH} \propto A \cdot \left[\frac{(\Delta H_{\text{HWHM}})^2 \cdot (H - H_{\text{res}})}{[(\Delta H_{\text{HWHM}})^2 + (H - H_{\text{res}})^2]^2} \right] + B \cdot \left[\frac{(\Delta H_{\text{HWHM}}) \cdot (H - H_{\text{res}})^2 - (\Delta H_{\text{HWHM}})^3}{[(\Delta H_{\text{HWHM}})^2 + (H - H_{\text{res}})^2]^2} \right]$, where A (B) is the amplitude of the field derivative of the symmetric (antisymmetric) Lorentzian function, μ_0H is the external d.c. magnetic field and $\mu_0\Delta H_{\text{HWHM}} = \frac{\sqrt{3}}{2}\mu_0\Delta H$ is the half-width-at-half-maximum (HWHM) of the imaginary part χ'' of the magnetic susceptibility.

From the linear scaling of $\mu_0\Delta H$ with f (Fig. 2a,b), we calculated the effective Gilbert(-type) damping constant α : $\mu_0\Delta H(f) = \mu_0\Delta H_0 + \frac{4\pi\alpha f}{\sqrt{3}\gamma}$, here $\mu_0\Delta H_0$ is the zero-frequency line broadening. We also estimated the effective saturation magnetization μ_0M_s (of the Ni_8Fe_2) from the dispersion relation of μ_0H_{res} with f (inset of Fig. 2a,b) using Kittel's formula: $f = \frac{\gamma}{2\pi} \sqrt{[\mu_0(H_{\text{res}} + M_{\text{eff}}) \cdot \mu_0H_{\text{res}}]}$, where $\gamma = g_L\mu_B/\hbar$ is the gyromagnetic ratio ($1.84 \times 10^{11} \text{ T}^{-1} \text{ s}^{-1}$), g_L is the Landé g -factor (taken to be 2.1), μ_B is the Bohr magneton and \hbar is Plank's constant divided by 2π .

For the iSHE (or transverse d.c. voltage) measurement³⁰, the sample was attached face down on the CPW by using an electrically insulating high-vacuum grease. A microwave signal was passed through the CPW and excited FMR of the Ni_8Fe_2 layer; a transverse d.c. voltage as a function of μ_0H was measured between two Ag-paste contacts at opposite ends of the sample. In these measurements, the microwave frequency was fixed at 5 GHz and the microwave power at the CPW at approximately 150 mW (for $T = 2$ and 8 K), which yields measurable signals (≥ 5 nV) in our setup.

The measured d.c. voltage (Fig. 3a,b) can be decomposed into symmetric and antisymmetric Lorentzian functions with respect to $\mu_0 H_{res}$, with weights of V_{sym} and V_{asy} respectively³⁰: $V(H) - V_0 = V_{sym} \cdot \left[\frac{(\Delta H')^2}{(\Delta H')^2 + (H - H_{res})^2} \right] + V_{asy} \cdot \left[\frac{(\Delta H') \cdot (H - H_{res})}{(\Delta H')^2 + (H - H_{res})^2} \right]$, where V_0 is a background voltage and $\mu_0 \Delta H'$ is the HWHM of the d.c. voltage. We attributed V_{sym} to the iSHE signal V_{iSHE} . If the Co thickness in the Pt/Co/Pt spin sink is larger than its spin dephasing length (a few ångstroms)³¹, $V_{iSHE}(\theta_{Co})$ is simply proportional to $\cos^2(\theta_{Co})$ (Fig. 3d).

Data availability

The data used in this paper can be accessed here (TBD).

References

33. Celinski, Z., Urquhart, K. B. & Heinrich, B. Using ferromagnetic resonance to measure the magnetic moments of ultrathin films. *J. Magn. Magn. Mater.* **166**, 6-26 (1997).

Figure legends

Figure 1. Principle of the approach and experimental setup **a**, Schematic of Pt(2.0 nm)/Co(t_{Co})/Pt(1.7 nm)/Nb(30 nm)/Ni₈Fe₂(6 nm)/Nb(30 nm)/Pt(1.7 nm)/Co(t_{Co})/Pt(2.0 nm) multilayers with different Co thicknesses t_{Co} . The Cu spacer with weak spin-orbit coupling (SOC) is selected to quench the interfacial Rashba-type SOC at the Nb/Pt/(Co/Pt) interface. **b**, Measurement scheme and Cartesian coordinate system used in the present study. **c**, Normalized resistance R/R_N vs. temperature T plots for three different sets of the samples, grown each in a single deposition run. **d**, t_{Co} dependence of

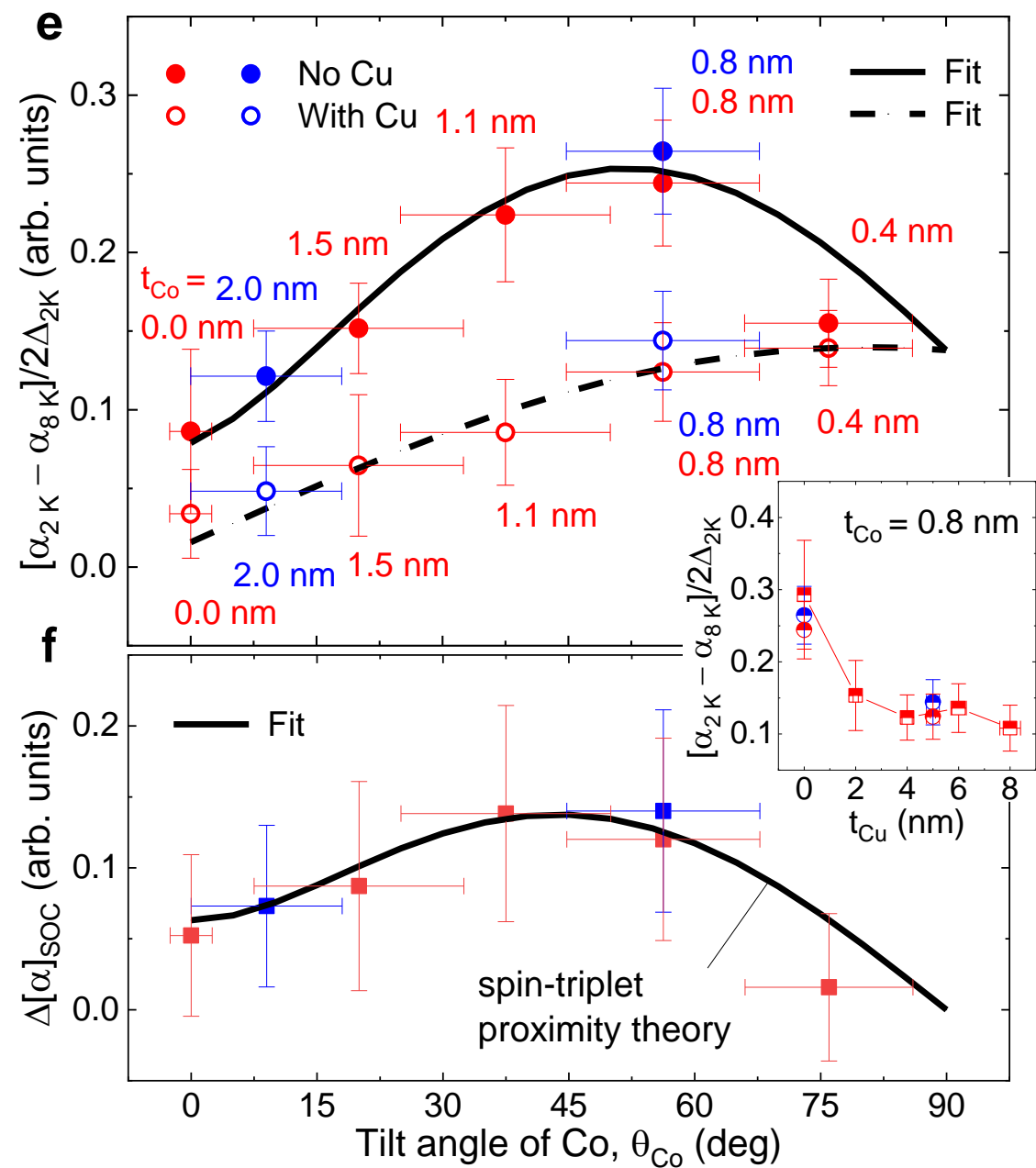
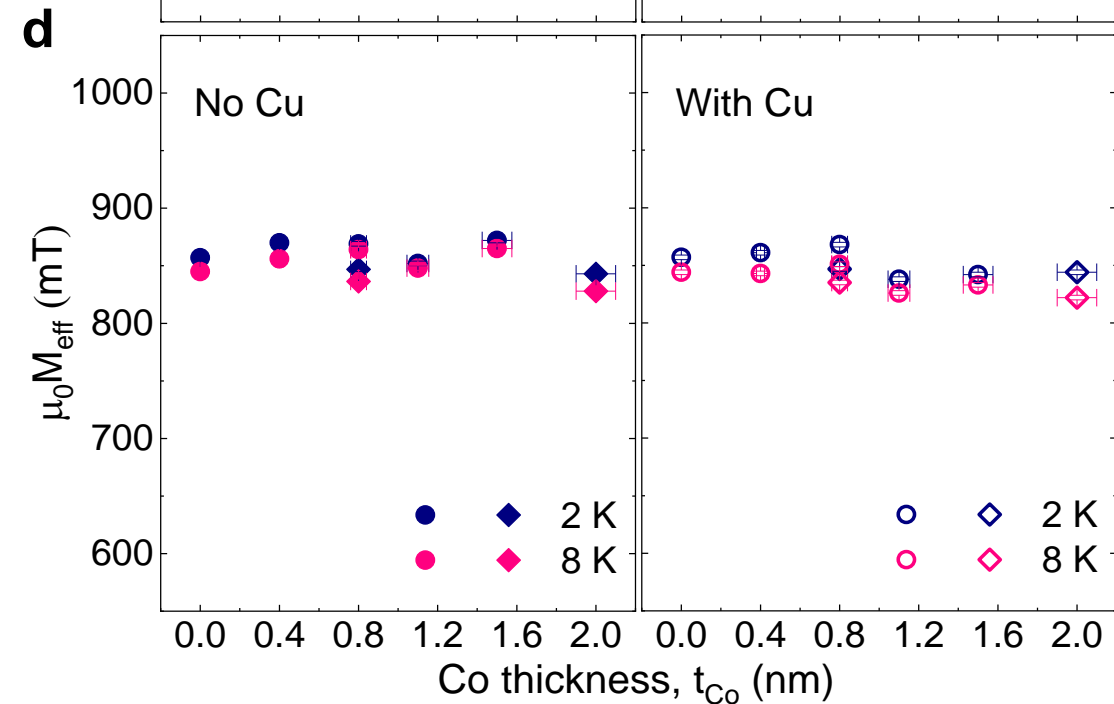
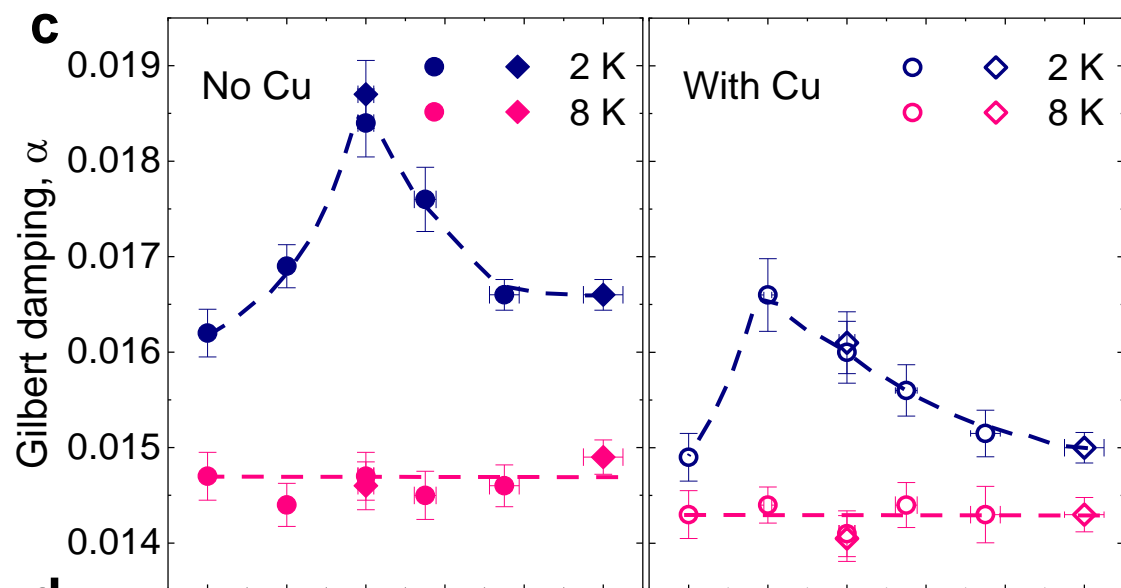
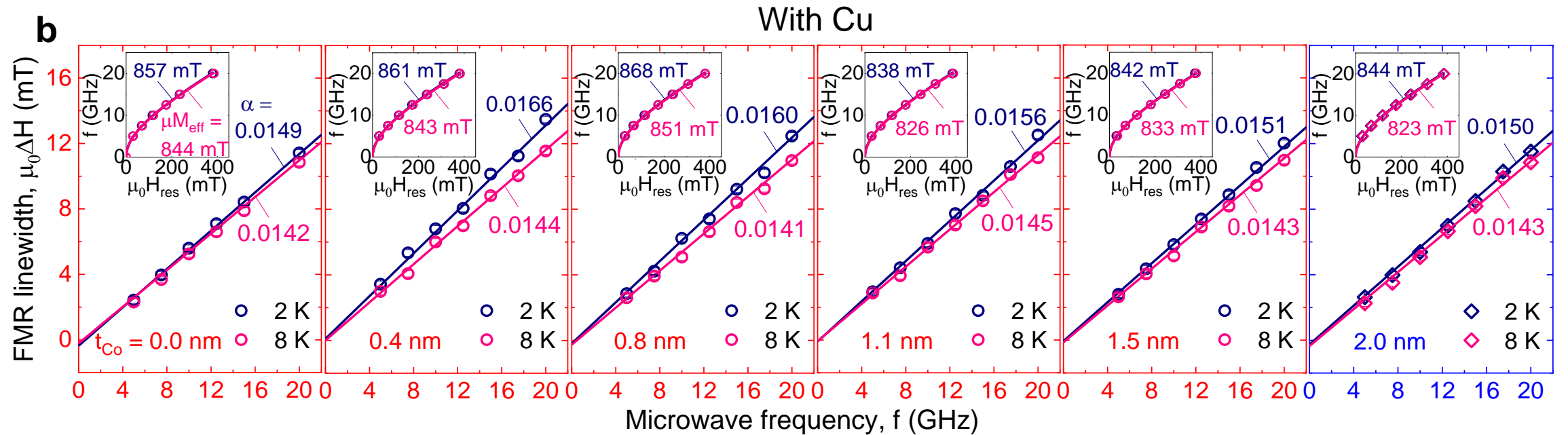
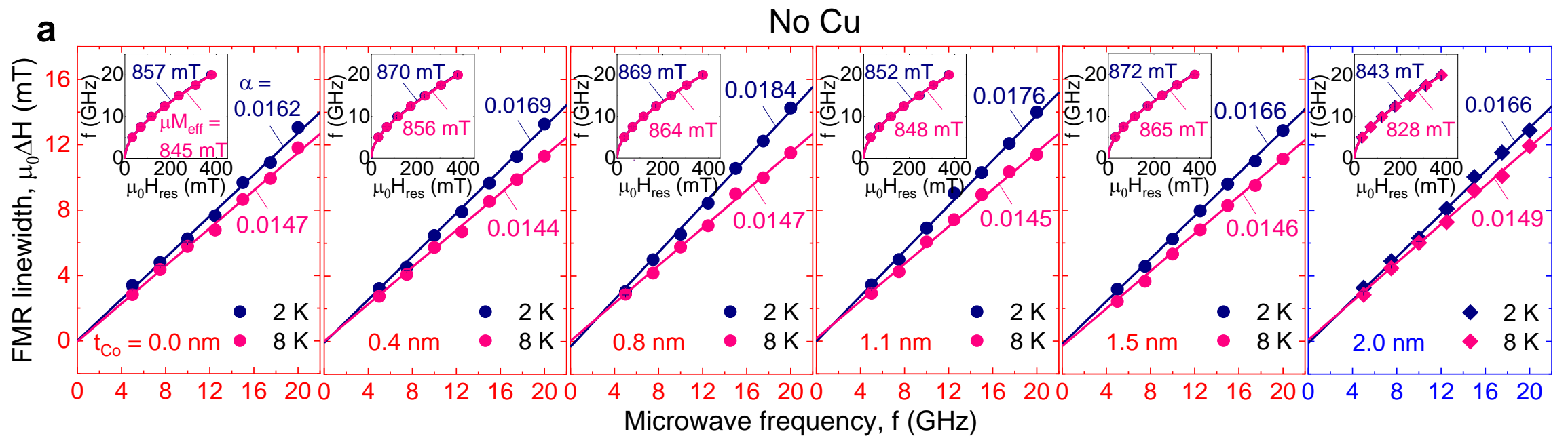
the superconducting transition temperature T_c of the sample sets with and without Cu(5 nm) spacer layers; for comparison, T_c of a bare Nb(30 nm) film is also shown. The black solid (dashed) line is a fit to estimate the effective values of coherence length and interface transparency (see Methods) for the Cu-absent (Cu-present) samples. **e**, In-plane and out-of-plane magnetization M curves of Pt(2.0 nm)/Co(t_{Co})/Pt(1.7 nm)/Nb(30 nm)-only films, measured at 8 K. **f**, Effective tilt angle θ_{Co} of the Co layer estimated from **e** using the Stoner-Wohlfarth model.

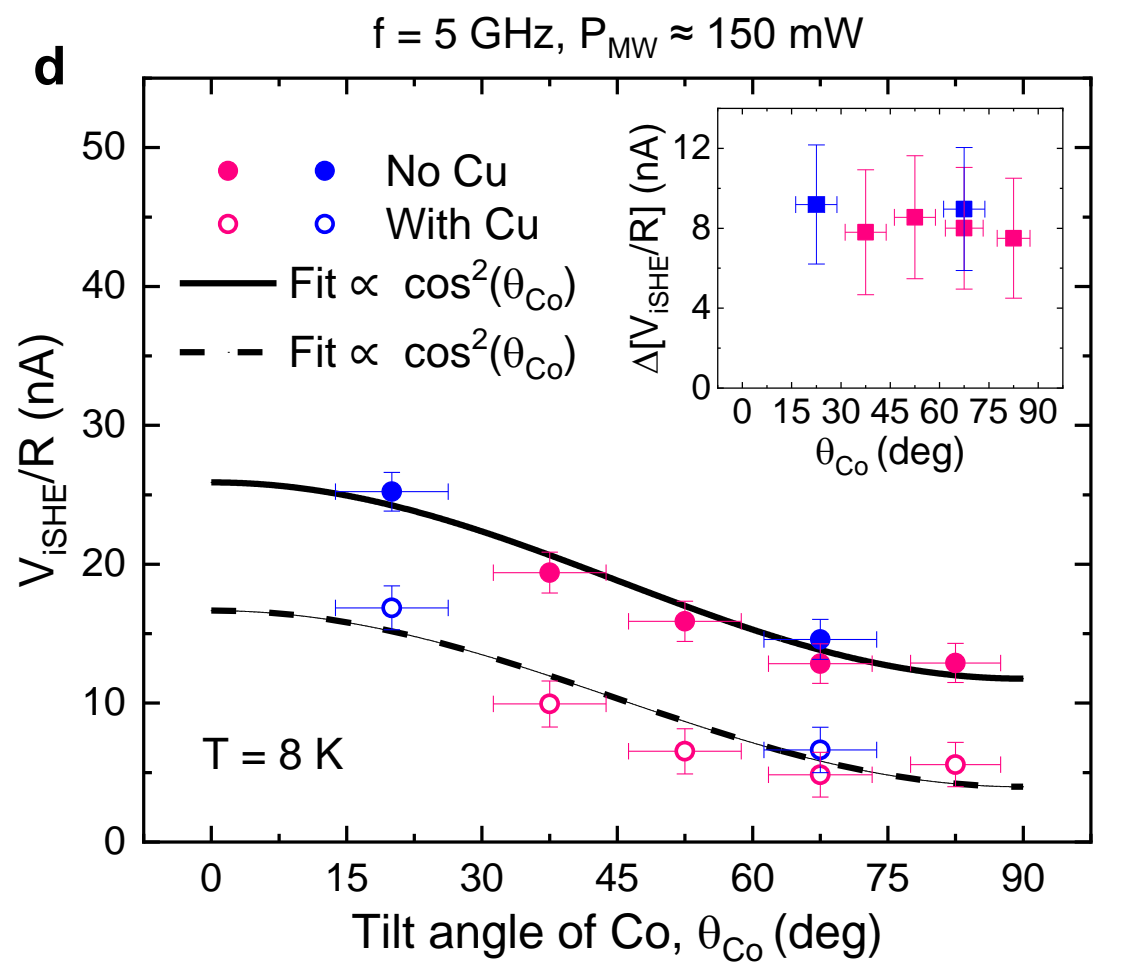
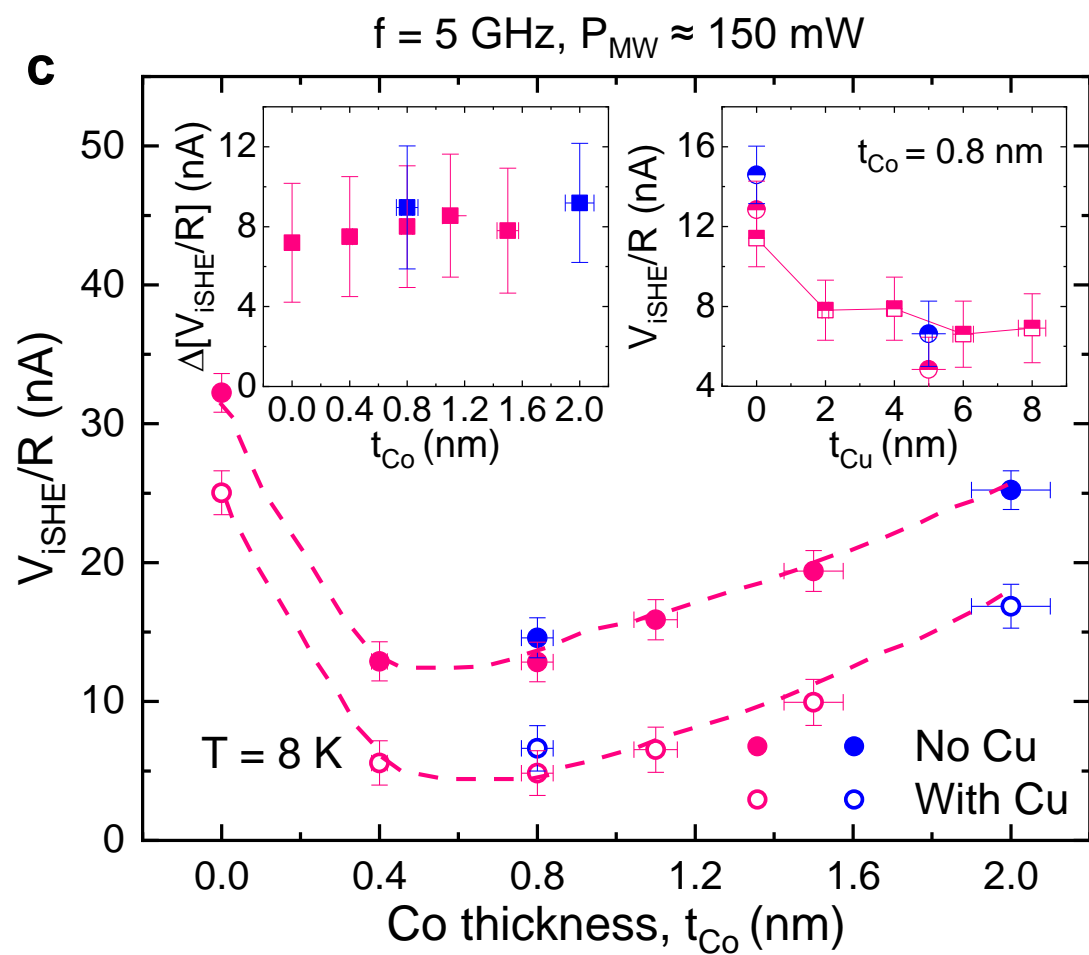
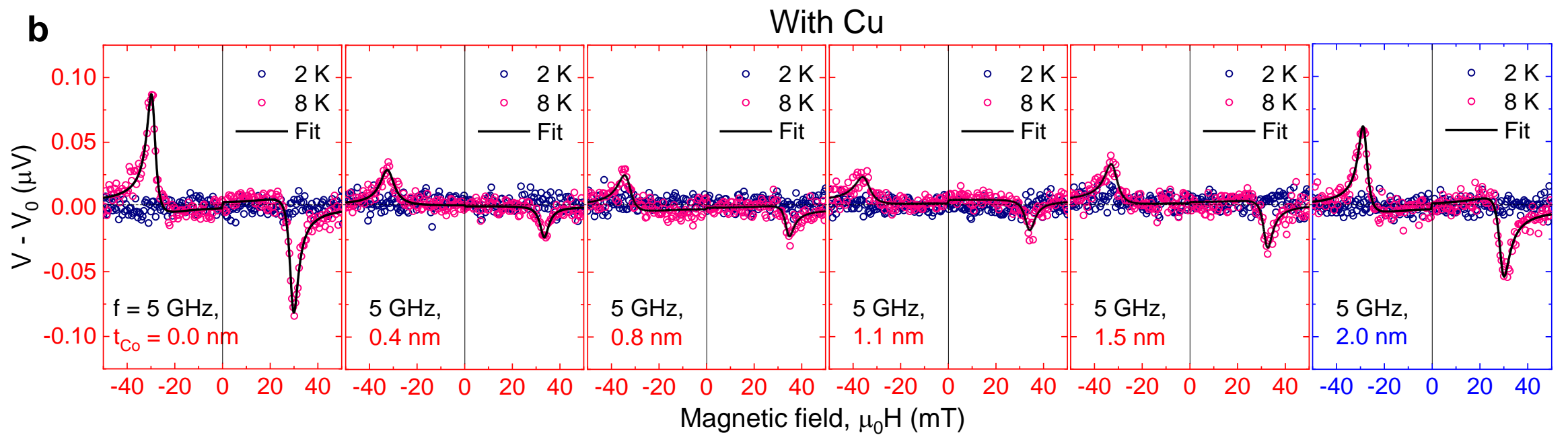
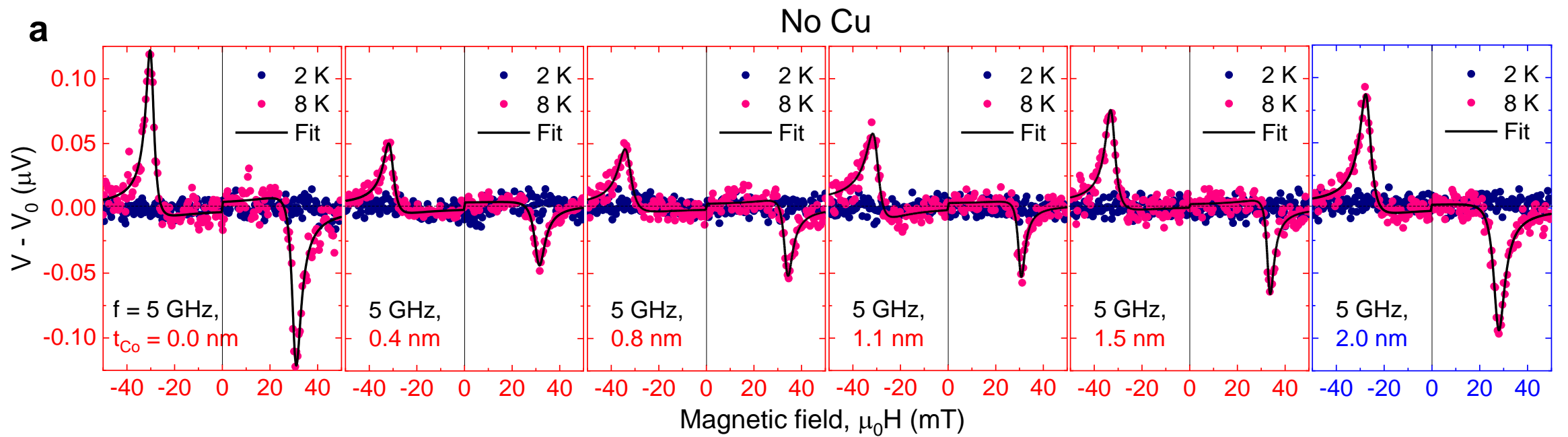
Figure 2. Correlation of Co tilt angle with superconducting spin-pumping efficiency.

a, Microwave frequency f dependence of ferromagnetic resonance (FMR) absorption for symmetric Pt(2.0 nm)/Co(t_{Co})/Pt(1.7 nm)/Nb(30 nm)/Ni₈Fe₂(6 nm)/Nb(30 nm)/Pt(1.7 nm)/Co(t_{Co})/Pt(2.0 nm) samples with various Co thicknesses, taken above and below T_c of the couple Nb. From this, one can extract the (effective) Gilbert(-type) damping α and the (effective) saturation magnetization $\mu_0 M_s$. **b**, Data equivalent to **a** but for symmetric Pt(2.0 nm)/Co(t_{Co})/Pt(1.7 nm)/Cu(5 nm)/Nb(30 nm)/Ni₈Fe₂(6 nm)/Nb(30 nm)/Cu(5 nm)/Pt(1.7 nm)/Co(t_{Co})/Pt(2.0 nm) samples. Extracted α (**c**) and $\mu_0 M_s$ (**d**) values as a function of t_{Co} for the samples with and without the Cu spacer. The dashed lines are guide to the eyes. **e**, Damping difference across T_c , denoted as $[\alpha_{2K} - \alpha_{8K}]/2\Delta_{2K}$ where 2Δ is the superconducting gap at 2 K calculated from the measured T_c (Fig. 1d), as a function of the (effective) Co tilt angle θ_{Co} . The black solid (dashed) line is a fit from spin-triplet proximity theory^{4,6,8} for the Cu-absent (Cu-present) samples (Supplementary Section 1,2). **f**, Interfacial SOC contribution $\Delta[\alpha]_{SOC}$, separated by taking the difference between the $[\alpha_{2K} - \alpha_{8K}]/2\Delta_{2K}$ data (**e**) with and without the Cu spacer. The black solid is a theoretical fit based on Rashba-type SOC-induced triplet pairing^{6,8} (Supplementary

Section 1,2). The inset of **e,f** shows $[\alpha_{2K} - \alpha_{8K}]/2\Delta_{2K}$ data as a function of Cu spacer thickness t_{Cu} for the $t_{Co}=0.8$ nm samples (Supplementary Section 4).

Figure 3. Effect of Cu spacer addition and Co tilt angle on normal spin-transport properties. **a**, Transverse d.c. voltage measurements for asymmetric Pt(2.0 nm)/Co(t_{Co})/Pt(1.7 nm)/Nb(30 nm)/Ni₈Fe₂(6 nm) samples with various Co thicknesses t_{Co} at a fixed microwave frequency $f = 5$ GHz, taken above and below T_c of the couple Nb. The black solid lines are fits to Lorentzian functions (see Methods). **b**, Data equivalent to **a** but for asymmetric Pt(2.0 nm)/Co(t_{Co})/Pt(1.7 nm)/Cu(5 nm)/Nb(30 nm)/Ni₈Fe₂(6 nm) samples. Inverse spin-Hall effect (iSHE) voltage divided by the sample's resistance V_{iSHE}/R as a function of t_{Co} (**c**) and the (effective) Co tilt angle θ_{Co} (**d**) at $f = 5$ GHz. The dashed lines are guide to the eyes. The left (right) inset in **c** (**d**) shows the signal difference caused by the Cu(5 nm) spacer addition whereas the right inset in **c** exhibits the Cu spacer thickness t_{Cu} dependence of iSHE for the $t_{Co}=0.8$ nm samples (see Supplementary Section 5 for details). The dashed lines in **c** are guide to the eyes whereas the black solid (dashed) line in **d** is a fit to $\cos^2(\theta_{Co})$ for the Cu-absent (Cu-present) samples.





Supplementary Information

Tunable creation of pure spin supercurrents via Rashba spin-orbit coupling with Pt/Co/Pt spin sinks

Kun-Rok Jeon,^{1,2*} Xavier Montiel,³ Chiara Ciccarelli,² Hidekazu Kurebayashi,⁴

Lesley F. Cohen,⁵ Sachio Komori,¹ Mark G. Blamire¹ and Jason W. A. Robinson^{1*}

¹*Department of Materials Science and Metallurgy, University of Cambridge, 27 Charles
Babbage Road, Cambridge CB3 0FS, United Kingdom*

²*Cavendish Laboratory, University of Cambridge, Cambridge CB3 0HE, United
Kingdom*

³*Department of Physics, Royal Holloway, University of London, Egham Hill, Egham,
Surrey TW20 0EX, United Kingdom*

⁴*London Centre for Nanotechnology and Department of Electronic and Electrical
Engineering at University of College London, London WC1H 0IH, United Kingdom*

⁵*The Blackett Laboratory, Imperial College London, SW7 2AZ, United Kingdom*

*To whom correspondence should be addressed: jeonkunrok@gmail.com,

jjr33@cam.ac.uk

This PDF file includes:

Supplementary Text

Figs. S1 to S5

References (S1-S17)

Section S1. Analytic description of the Co tilt angle dependence of equal-spin triplet pairing.

To support our interpretation theoretically, we first consider a simple analytic form for the proximity generation of spin-polarized triplet supercurrents (or equal-spin triplet pairs) J_s^{eq} . We speculate that when the equal-spin triplet pairs are present in our proximity-coupled system, a new *equilibrium* channel opens for pumped spin currents from precessing magnetization to be transferred through a singlet superconductor to Pt spin sink, giving rise to the enhanced spin pumping/transfer (see Section S2 for further discussion). As described in the main text, there are two distinct origins of J_s^{eq} in our experimental setup: 1) the magnetization noncollinearity^{S1-S3} between Ni₈Fe₂ (= Py) and Co layers, J_{s1}^{eq} , and 2) the spin-orbit coupling (SOC)^{S4-S8} in combination with a magnetic exchange field h_{ex} at a Nb/Pt/(Co/Pt) interface, J_{s2}^{eq} .

In the first mechanism, irrelevant to the SOC, it has been shown that J_{s1}^{eq} scales with the relative magnetization angle $\theta (= \theta_{Co} - \theta_{Py})$ between the two FMs, or equivalently, the cross product of magnetization vectors (\mathbf{M}_{Co} , \mathbf{M}_{Py}) of the two FMs^{S1-S3}:

$$J_{s1}^{eq} \propto \mathbf{M}_{Co} \times \mathbf{M}_{Py} \propto \sin(\theta). \quad (S1)$$

The second SOC mechanism predicts that at the Nb/Pt/(Co/Pt) interface, J_{s2}^{eq} scales with the cross product of the SO vector operator $[\hat{A}_k, [\hat{A}_k, h^a \sigma^a]]$ and the exchange field operator $h^a \sigma^a$, that is, the degree of orthogonality between SOC and h_{ex} ^{S4-S8}:

$$J_{s2}^{eq} \propto h^a \sigma^a \times [\hat{A}_k, [\hat{A}_k, h^a \sigma^a]], \quad (S2)$$

where $\hat{A}_{k=x,y,z}$ is the vector potential describing the form of SOC, e.g., the Rashba constant α_R (Dresselhaus constant β_D) due to the interface (bulk) inversion asymmetry.

$\sigma^a(h^a)$ with $a = x,y,z$ is the vector of Pauli (exchange field) matrices.

For a metallic vertical structure with *non-ideal* interfaces where the OOP component α_a of the Rashba SO field relative to the local interface plane survives *on a scale of the superconducting coherence length*^{S7}, the vector potential can be approximately generalized as:

$$\hat{A}_x \approx \alpha_a \sigma^a, \hat{A}_y \approx -\beta_D \sigma^y + \alpha_R \sigma^z, \hat{A}_z \approx \beta_D \sigma^z - \alpha_R \sigma^y. \quad (\text{S3})$$

Assuming finite Rashba ($\alpha_R \neq 0$) and zero Dresselhaus ($\beta_D = 0$) contribution to the SOC^{S6,S8}, as relevant to our experimental setup, we obtain the following SO vector operator:

$$\begin{aligned} \left[\hat{A}_k, [\hat{A}_k, h^a \sigma^a] \right] \approx & \left[(8\alpha_R^2 + 4\alpha_y^2 + 4\alpha_z^2)h^x - 4\alpha_x \alpha_y h^y - 4\alpha_z \alpha_x h^z \right] \sigma^x + \\ & \left[(4\alpha_R^2 + 4\alpha_z^2 + 4\alpha_x^2)h^y - 4\alpha_y \alpha_z h^z - 4\alpha_x \alpha_y h^x \right] \sigma^y + \left[(4\alpha_R^2 + 4\alpha_x^2 + \right. \\ & \left. 4\alpha_y^2)h^z - 4\alpha_z \alpha_x h^x - 4\alpha_y \alpha_z h^y \right] \sigma^z. \quad (\text{S4}) \end{aligned}$$

Notably, it is evident from Eq. (S4) that if at least two of α_a are non-zero, the SO vector operator $\left[\hat{A}_k, [\hat{A}_k, h^a \sigma^a] \right]$ has a component orthogonal to the exchange field operator $h^a \sigma^a$ even with a purely IP magnetized FM ($h^x = 0$)^{S7}, thereby producing the finite J_{s2}^{eq} . This is a likely mechanism^{S7} that explains how we could have observed the enhanced spin-pumping efficiency in the superconducting state for our previous FMR experiments^{S9,S10} and for the $t_{Co} = 0$ samples (Fig. 2e).

Using Eq. (S1)-(S4) and assuming that the Cu(5 nm) spacer addition at the Nb/Pt/(Co/Pt) interface reduces the interfacial Rashba SOC strength^{S11,S12} (α_R , $\alpha = \sqrt{\alpha_x^2 + \alpha_y^2 + \alpha_z^2}$) by a factor of 7, we can successfully reproduce the FMR results (Fig. 2e,f). Note that in this calculation, we ignored the Cu(5 nm) addition effect on J_{s1}^{eq} as the thickness used is about 2 orders of magnitude smaller than its coherence length. Figure

S1a shows the calculated total J_s^{eq} ($= J_{s1}^{eq} + J_{s2}^{eq}$) as a function of the Co tilt angle θ_{Co} with respect to the global interface plane, which is parallel to the M_{Py} direction θ_{Py} . The SOC contribution, isolated by taking the difference in J_s^{eq} due to the Cu spacer addition; $J_s^{eq, no Cu} - J_s^{eq, with Cu}$, is also displayed in Fig. S1b.

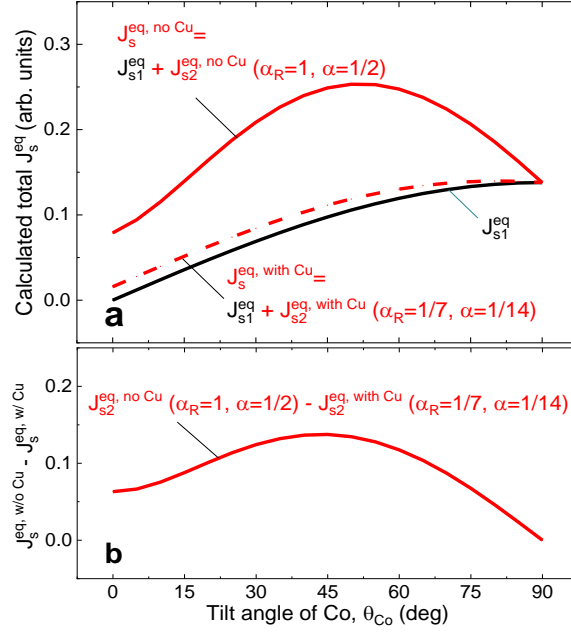


Figure S1. Calculated spin-polarized triplet supercurrents versus Co tilt angle **a**, total J_s^{eq} ($= J_{s1}^{eq} + J_{s2}^{eq}$) as a function of the Co tilt angle θ_{Co} calculated using Eq. (S1)-(S4). **b**, Difference in J_s^{eq} due to the Cu spacer addition ($J_s^{eq, no Cu} - J_s^{eq, with Cu}$), indicating the interfacial SOC contribution, is shown versus θ_{Co} . These are identical to presented the solid and dashed black lines in Fig. 2e,f (main text).

Section S2. Numerical calculation based on the Usadel formalism.

In this section, we present the calculation of the triplet correlations in a simplified version of the Pt/Co/Pt/Nb/Py/Nb/Pt/Co/Pt multilayer.

We modelize the Py layer as a ferromagnetic layer F with a small internal exchange field h^{Py} and the Nb layer as a singlet superconducting layer S described by the order parameter Δ^{SC} . In the experiment, the Pt/Co/Pt trilayer is composed by thin Pt and Co

layers with transparent Pt/Co interfaces. Therefore, we can modelize the Pt/Co/Pt trilayer as a unique ferromagnetic layer with an internal spin-orbit coupling: the Fso layer. This Fso layer exhibits an internal exchange field h^{Fso} as well as a spin-orbit coupling field A_{SO} . In the following, we will consider that the Fso layer exhibits a canted magnetization compared to the F layer one. The initial multilayer is then simplified as a Fso/S/F/S/Fso pentalayer. The experimental multilayer is symmetric. Therefore, we can further simplify the pentalayer by a F/S/Fso trilayer.

The Usadel formalism. In order to calculate the spin triplet correlation and the spin current in the F/S/Fso trilayer, we solve the Usadel equations at equilibrium^{S2,S11,S12}. This formalism proposes a quasi-classical description of the superconductivity in the diffusive regime. At equilibrium, the Usadel equation writes^{S2,S11,S12}

$$[E\hat{\tau}_3 - \hat{\Sigma}, \hat{G}] + \frac{D}{\pi} \nabla(\hat{G} \nabla \hat{G}) = 0 \quad (\text{S5})$$

where $\hat{G}(E, \mathbf{R})$ are the Green function in the 4×4 spin \times particle-hole space (or spin-resolved Nambu space) depending on the energy E and space coordinate \mathbf{R} . D is the diffusive coefficient and $\hat{\Sigma}$ are the self-energy describing the physics in each layer. In the spin \times particle-hole space, we write the Green functions along the Nambu spinor $\Psi = (\psi_{\uparrow}, \psi_{\downarrow}, \psi_{\uparrow}^{\dagger}, \psi_{\downarrow}^{\dagger})$. In the particle-hole space, the Green function writes $\hat{G} = \begin{pmatrix} g & f \\ \tilde{f} & \tilde{g} \end{pmatrix}$ where g and \tilde{g} are the normal Green function in the spin space and f and \tilde{f} are the anomalous Green function in the spin space. The transformation $\tilde{\cdot}$ denotes the complex conjugation operation associated with the transformation $E \rightarrow -E$.

In the F layer, the self-energy writes in the spin \times particle-hole space:

$$\hat{\Sigma}^F = \begin{pmatrix} \mathbf{h}^F \boldsymbol{\sigma} & 0 \\ 0 & \mathbf{h}^F \boldsymbol{\sigma}^* \end{pmatrix} \quad (\text{S6})$$

with h^F is the internal exchange field in the F layer and $\boldsymbol{\sigma}$ the Pauli matrices vector. In the following, we consider that the magnetization in the F layer is directed along the z axis.

In the Fso layer, the self-energy writes

$$\hat{\Sigma}^{Fso} = \begin{pmatrix} \mathbf{h}^{Fso} \boldsymbol{\sigma} & 0 \\ 0 & \mathbf{h}^{Fso} \boldsymbol{\sigma}^* \end{pmatrix} \quad (S7)$$

where \mathbf{h}^{Fso} is the internal exchange field in the Fso layer. In the following, we consider that the magnetization in the Fso layer is canted from the z -axis along the x -axis by an angle θ .

In the Fso layer, we consider the linear in momentum spin-orbit coupling by replacing the initial space derivative by the covariant space derivative^{S4,S5,S7}: $\bar{\nabla} \rightarrow \nabla - i[\hat{\underline{A}}]$. The SOC field structure in the spin \times particle-hole space is $\hat{\underline{A}} = \begin{pmatrix} \underline{A} & 0 \\ 0 & -\underline{A}^* \end{pmatrix}$ and $\underline{A} = \begin{pmatrix} A_x \\ A_y \\ A_z \end{pmatrix}$. The SOC provides coupling between the different triplet component of the anomalous Green functions and then implies a spin rotation process in the F/S/Fso trilayer which can generate long-range triplet correlations^{S4,S5,S7}.

In the superconducting layer, the self-energy writes:

$$\hat{\Delta}^R = \begin{pmatrix} 0 & \Delta^{SC} \\ \widetilde{\Delta}^{SC} & 0 \end{pmatrix} \quad (S8)$$

The superconducting order parameter as to be determined from the self-consistency equation:

$$\Delta^{SC}(\mathbf{x}) = \lambda \int_{-E_c}^{+E_c} \frac{dE}{2i\pi} f_s(E, \mathbf{x}) \tanh\left(\frac{E}{2T}\right) \quad (S9)$$

where f_s is the singlet part of the anomalous Green function (see for example the definition in ^{S2,S7}) and T is the temperature. The inner interfaces are described by the

Nazarov boundary conditions^{S13}. The F and the Fso layer outer interfaces are described by the condition $\nabla\hat{G} = 0$ and $\bar{\nabla}\hat{G} = 0$ respectively.

We further simplify the multilayer by considering that each monolayer extent infinitely in the (y-z) plane perpendicular to the stack axis \mathbf{x} . Therefore, the initial spatial derivative simplifies as $\nabla \rightarrow \frac{\partial}{\partial x}$ and the Green function only depends on the x coordinate $\hat{G}(\mathbf{E}, \mathbf{R}) \equiv \hat{G}(\mathbf{E}, x)$.

We solve the one-dimensional Usadel equation by considering the Riccati matrix parametrization^{S7}. From this numerical solution, we can compute the spin current flowing along the multilayer stack axis x which expresses as^{S7}:

$$I_{xs} = J_{s0} \text{Re} \int \frac{dE}{4\pi^2} \text{Tr}(\hat{\tau}_3 \hat{\sigma} \hat{G} \partial_x \hat{G}) \tanh\left(\frac{E}{2T}\right) \quad (\text{S10})$$

where $J_{s0} = -\frac{\hbar N_0 D}{2}$, \hbar is the Reduced Planck constant and N_0 is the density of state at the Fermi level. Here, the spin current exhibits three components in the spin space related to each Pauli matrices

$$I_x^{s,i} = J_{s0} \text{Re} \int \frac{dE}{4\pi^2} \text{Tr}(\hat{\tau}_3 \hat{\sigma}^i \hat{G} \partial_x \hat{G}) \tanh\left(\frac{E}{2T}\right). \quad (\text{S11})$$

with $i = \{x, y, z\}$. In the following, we present the module of the total spin current $|I_x^s| =$

$$\sqrt{|I_x^{s,x}|^2 + |I_x^{s,y}|^2 + |I_x^{s,z}|^2}.$$

Results. The equilibrium spin current is a good indicator of the presence of long-range correlations in a multilayered system^{S6,S7}. Moreover, this superconducting pure spin current only exists below the critical temperature.

Regarding the component A_y and A_z of the SOC fields, we have considered the spin-orbit coupling symmetry defined in the relation (S3). Along the x axis, we consider

the SOC symmetry studied in the reference^{S7} ($\alpha = \alpha_x$) for simplicity and writing $A_x = \alpha\sigma^x$.

The profile of the spin current intensity for different canting angle θ and different spin-orbit coupling symmetry is shown in Fig. S2A (the parameter are provided in the figure caption). We observe that the spin current is constant in the S layer because of spin-flip immunity in the S layer^{S6}. In the F and Fso layers, the space dependency of the spin current originates the oscillations of the triplet correlations coming from the canted exchange fields^{S4,S5,S7} or induced by the spin-orbit coupling^{S4,S5,S7}.

The canting angle dependency of the spin current in the middle of the S and the Fso layer is shown in Fig. S2B. Inside the S layer, the pure spin current is minimal for aligned magnetization $\theta = 0$ while it is maximal for orthogonal configuration $\theta = \pi/2$. In the Fso layer, the spin current profile depends on the symmetry of the spin-orbit coupling. Note that in the case of a Rashba spin-orbit coupling (Fig. S2Bb), the spin current in the Fso layer is maximal for $\theta \approx \pi/4$. Note that in the presence of the SOC symmetry considered in the paper^{S7}, the spin current is non-zero for in-plane aligned magnetization (Fig. S2Bc).

This superconducting spin current can be understood as an *equilibrium* torque originating from equal-spin triplet Cooper pairs generated by both F layer magnetization and SOC^{S7}. In the FMR experiment, a *non-equilibrium* spin current pumped from precessing F can be understood in terms of a *damping* torque, which would have a component from the misalignment between the induced exchange field, which is rotated due to the spin-orbit coupling, in Pt and the magnetization in Ni₈Fe₂. In addition, it would be *proportional* to the amount of equal-spin pairs that can transport spin-angular-momentum across the superconductor into the spin loss regions. Consequently, the

precession induced in the Py layer is sensible to the equilibrium torque provided by the triplet correlation produced in the whole multilayer. Note that the equal-spin triplet is a ground state property and thus it does not exert a damping torque but an equilibrium torque. In order to quantify the overall effect of the triplet correlations on the F precession, we have integrated the spin current in the full F/S/Fso layer in order to quantify the general equilibrium spin torque $\tau^{int} = \int_0^L |I_x^s| dx$ shown in Fig. S2C.

We also simulate the angular dependence of τ^{int} in the presence of the Cu layer with the reduced (effective) magnitude of the SOC field by a factor of 10 (see Fig. S2D). The calculated angular dependence of the integrated torque is qualitatively identical to the experimental results (Fig. 2e, main text).

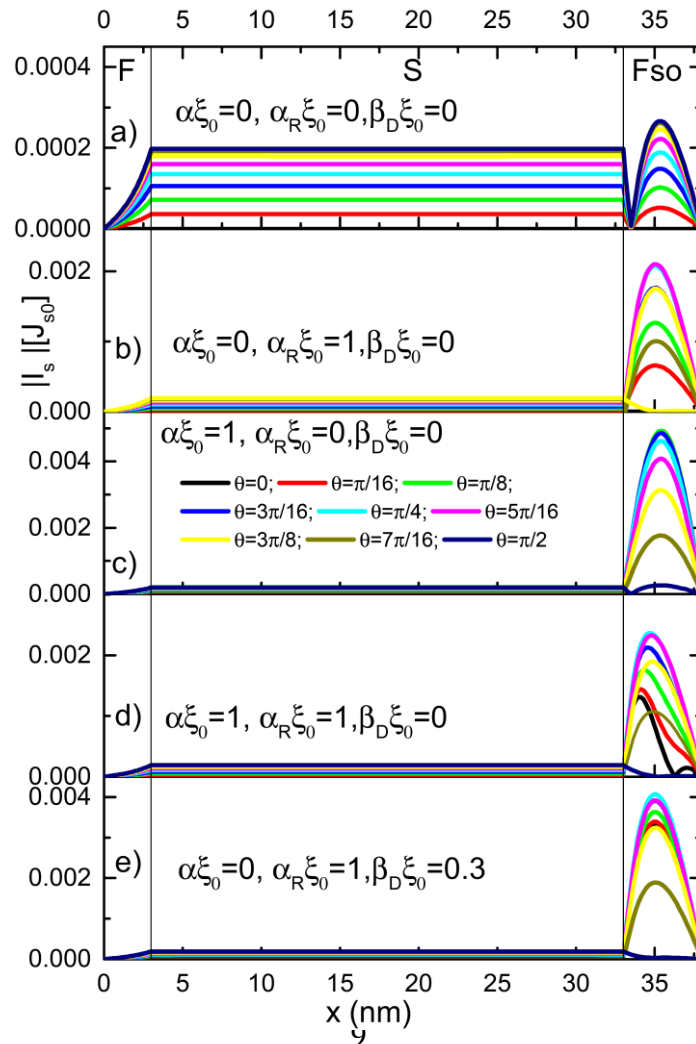


Figure S2A. The spin current profile in the F/S/Fso trilayer for different spin-orbit coupling symmetry and canting angle θ . The layer thicknesses are $d_F = 3nm$, $d_S = 30nm$ and $d_{Fso} = 5nm$ with $\xi_0 = \sqrt{D/\Delta_0}$ the superconducting coherence length equals to 13nm. The exchange field magnitude is $h_F = 5\Delta_0$ and $h_{Fso} = 10\Delta_0$ while the transparency at both F/S and S/Fso interfaces is set at $t = 0.5$. The calculations are done at small temperature $T = 0.01\Delta_0$.

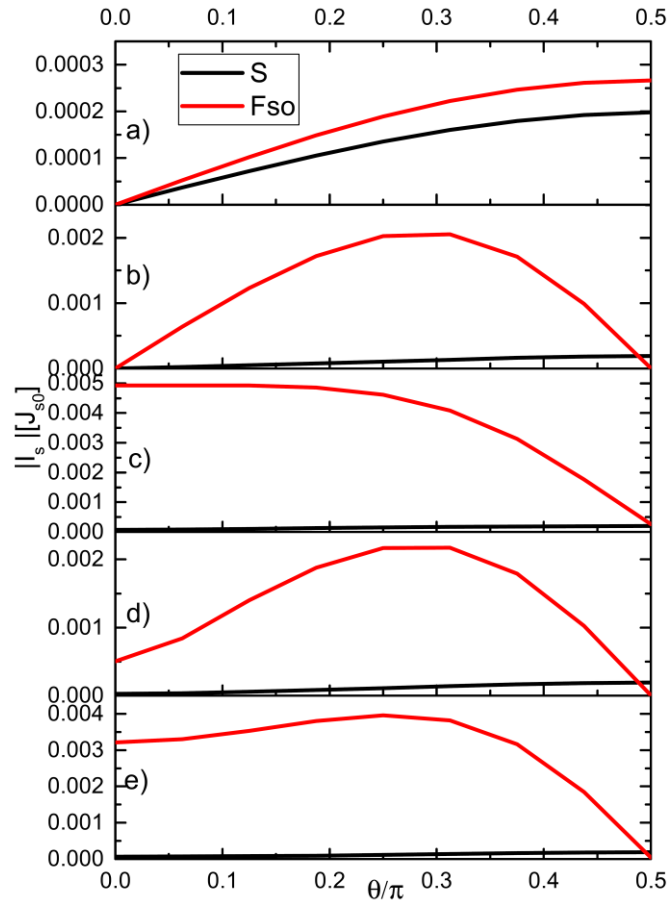


Figure S2B. Canting angle dependence of the spin current magnitude in the middle of the S layer (black) and in the middle of the Fso layer (red) for different SOC symmetry. The parameters are the same than in Fig. S2A.

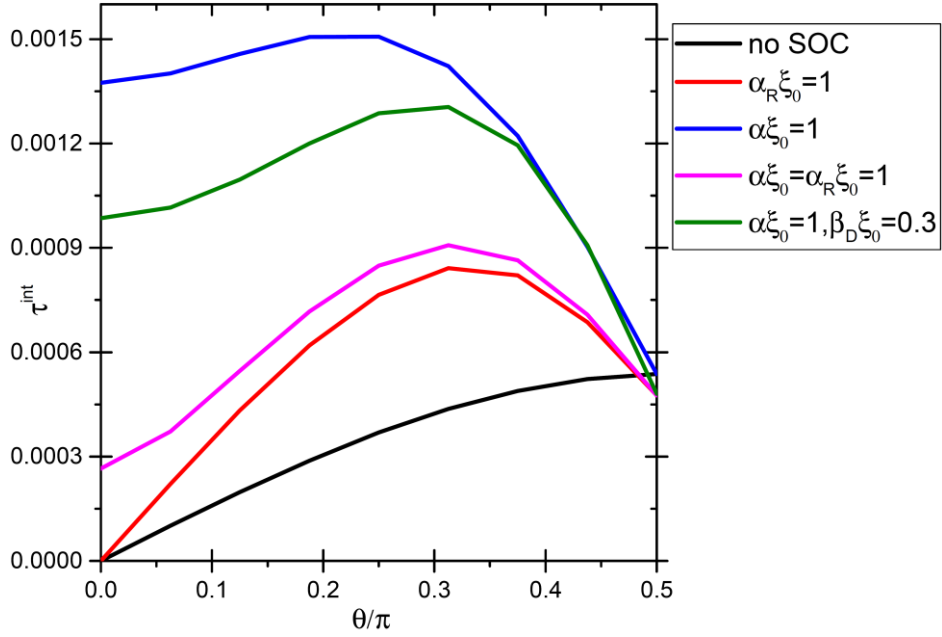


Figure S2C. Canting angle dependence of the integrated torque for different SOC symmetry. The parameters are the same than in Fig. S2A.

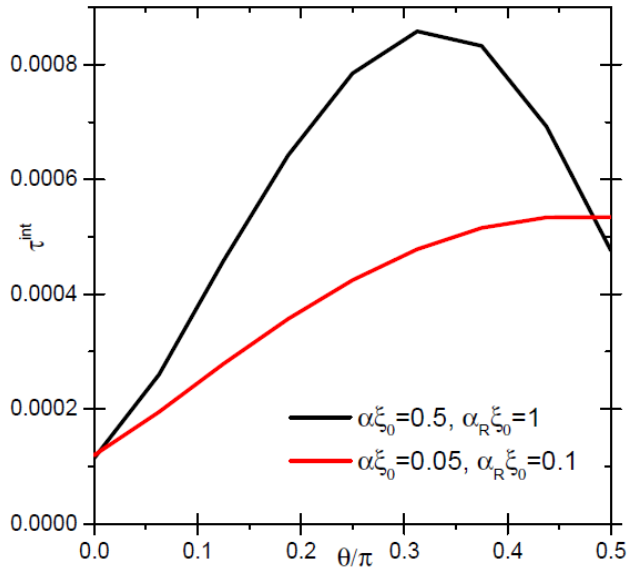


Figure S2D. Effect of Cu spacer addition on the canting angle dependence of the integrated torque. The other parameters are the same than in Fig. S2A. The black line represents the angle dependence τ^{int} when no Cu layer exists in the multilayer. The red line simulates the effect of the Cu layer by dividing the magnitude of the SOC by 10. In both cases, the calculated angular dependence of τ^{int} is qualitatively the same as the experimental results (Fig. 2e, main text)

Section S3. FMR spectra for Pt/Co/Pt/Nb/Ni₈Fe₂/Nb/Pt/Co/Pt samples with and without Cu spacers.

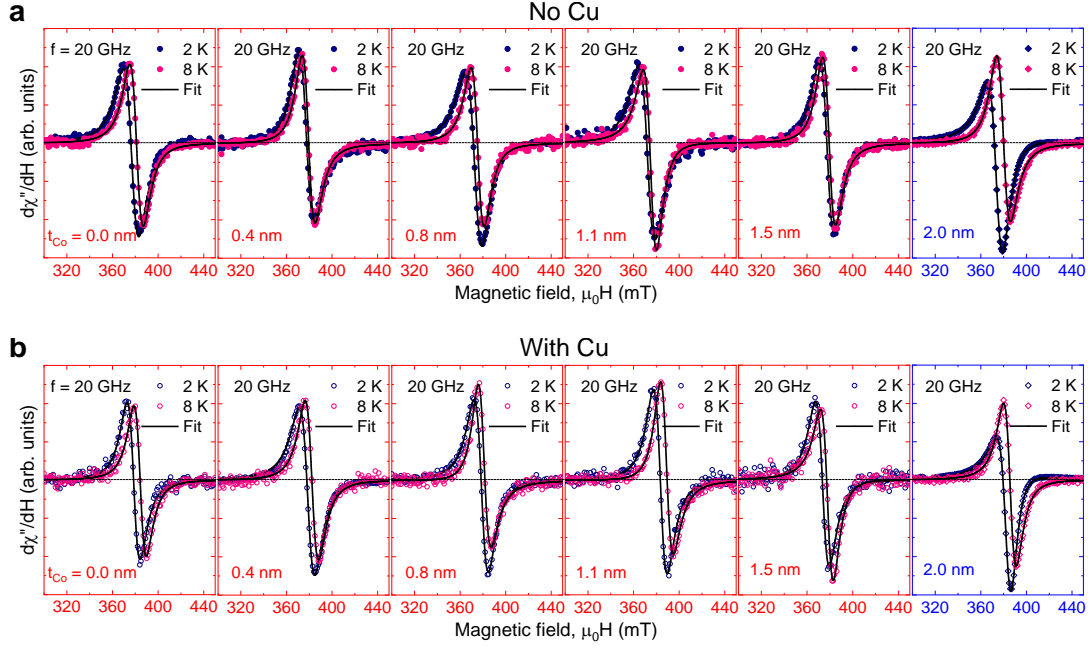
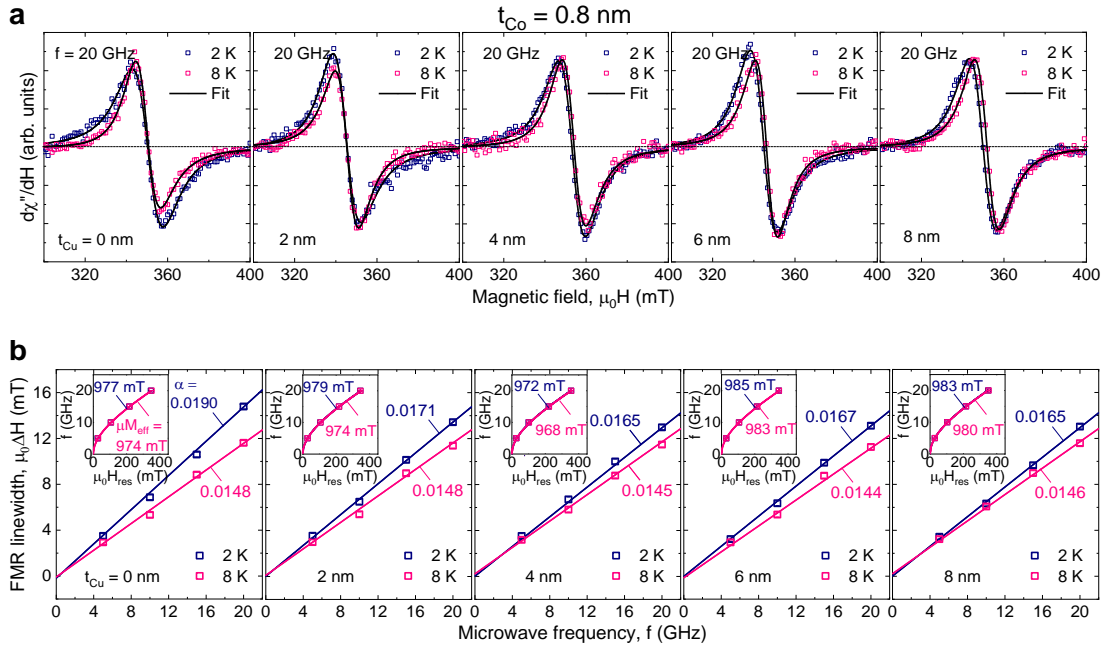


Figure S3. Analysis of FMR absorption spectra. a, Typical FMR spectra of symmetric Pt(2.0 nm)/Co(t_{Co})/Pt(1.7 nm)/Nb(30 nm)/Ni₈Fe₂(6 nm)/Nb(30 nm)/Pt(1.7 nm)/Co(t_{Co})/Pt(2.0 nm) samples with various Co thicknesses t_{Co} at a fixed microwave frequency $f = 20$ GHz, taken above and below T_c of the couple Nb. The black lines are fits to the field derivative of Lorentzian functions in order to determine the FMR linewidth $\mu_0\Delta H$ and the resonance magnetic field μ_0H_{res} (see Methods). **b,** Data equivalent to **a** but for symmetric Pt(2.0 nm)/Co(t_{Co})/Pt(1.7 nm)/Cu(5 nm)/Nb(30 nm)/Ni₈Fe₂(6 nm)/Nb(30 nm)/Cu(5 nm)/Pt(1.7 nm)/Co(t_{Co})/Pt(2.0 nm) samples. From **a,b**, the data presented in Fig. 2 a,b of the main text was, respectively, extracted.

Section S4. Cu spacer thickness dependence of superconducting spin-pumping efficiency.

In this section, we investigate how the superconducting-state damping enhancement scales with the Cu spacer thickness t_{Cu} to further identify the underlying mechanism behind the observed characteristic angular dependence: i.e. Rashba-type SOC at the

Nb/Pt/(Co/Pt) interface. Applying the same FMR approach as for the two sample sets with and without the Cu(5 nm) spacer (see Fig. 2, main text) to symmetric Pt(2.0 nm)/Co(0.8 nm)/Pt(1.7 nm)/Cu(t_{Cu})/Nb(30 nm)/Ni₈Fe₂(6 nm)/Nb(30 nm)/Cu(t_{Cu})/Pt(1.7 nm)/Co(0.8 nm)/Pt(2.0 nm) samples (Fig. S4a-d), we obtain the FMR damping α difference across the superconducting transition temperature T_c , denoted as $[\alpha_{2\text{K}} - \alpha_{8\text{K}}]/2\Delta_{2\text{K}}$, vs. t_{Cu} (Fig. S4e). Obviously, even for very thin Cu spacers (≤ 8 nm) whose thickness is around 2 orders of magnitude smaller than either the coherence length or the spin diffusion length^{S15}, the superconducting-state damping enhancement ($[\alpha_{2\text{K}} - \alpha_{8\text{K}}]/2\Delta_{2\text{K}} > 0$) dramatically decreases with increasing t_{Cu} . This strongly supports that the characteristic angular dependence observed in our experiments basically originates from the Rashba SOC at the interface of Nb/Pt/(Co/Pt) layers^{S6,S8}.



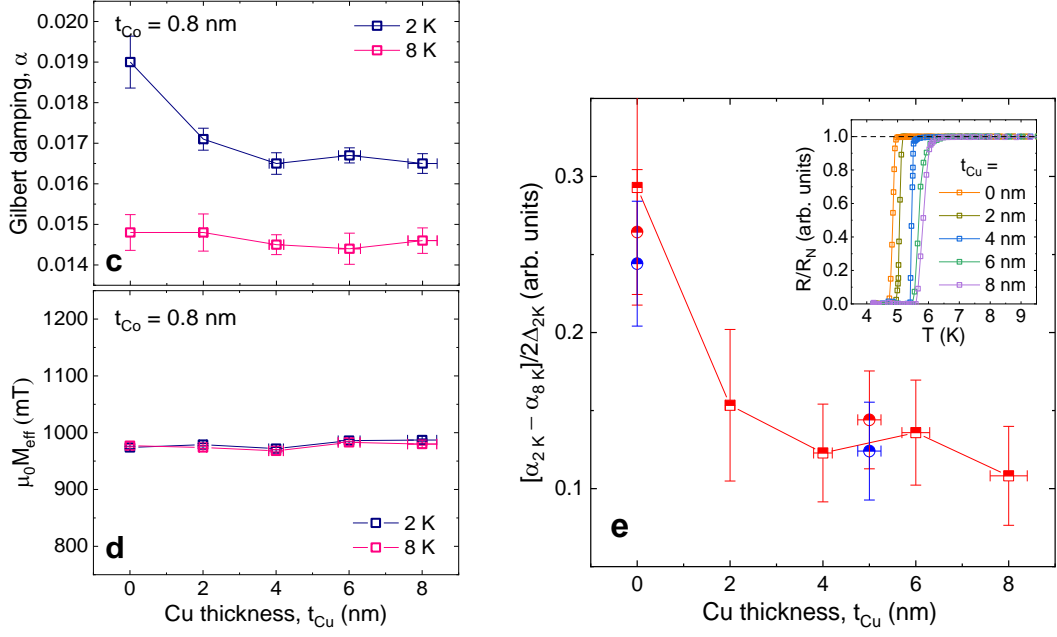


Figure S4. Strong suppression of superconducting-state damping enhancement by the presence of a few-nm-thick Cu spacer. Representative FMR spectra of symmetric Pt(2.0 nm)/Co(0.8 nm)/Pt(1.7 nm)/Cu(t_{Cu})/Nb(30 nm)/Ni₈Fe₂(6 nm)/Nb(30 nm)/Cu(t_{Cu})/Pt(1.7 nm)/Co(0.8 nm)/Pt(2.0 nm) samples with various Cu thicknesses t_{Cu} at a fixed microwave frequency $f = 20$ GHz, taken above and below the superconducting transition temperature T_c of the couple Nb. The black lines are fits to the field derivative of Lorentzian functions (see Method). **b**, Associated f dependence of FMR data from which one can extract the (effective) Gilbert(-type) damping α and the (effective) saturation magnetization $\mu_0 M_s$. Extracted α (**c**) and $\mu_0 M_s$ (**d**) values as a function of t_{Cu} for the control samples. **e**, Damping difference across T_c , denoted as $[\alpha_{2\text{K}} - \alpha_{8\text{K}}]/2\Delta_{2\text{K}}$ where 2Δ is the superconducting gap at 2 K calculated from the measured T_c (inset), as a function of t_{Cu} .

Section S5. Cu spacer thickness dependence of normal spin-transport properties.

For completeness, we also perform the t_{Cu} dependence of spin-pumping-induced iSHE (see Methods for details) for asymmetric Pt(2.0 nm)/Co(0.8 nm)/Pt(1.7 nm)/Cu(t_{Cu})/Nb(30 nm)/Ni₈Fe₂(6 nm) structures (Fig. S5a). A visible decay of iSHE signals at 8 K (or normal spin-transport data) with the increase of t_{Cu} (Fig. S5b) can also

be explained in the context of the quenched Rashba-type SOC caused by the Cu spacers^{S16,S17} and thereby the reduced (effective) spin-to-charge conversion^{S17}.

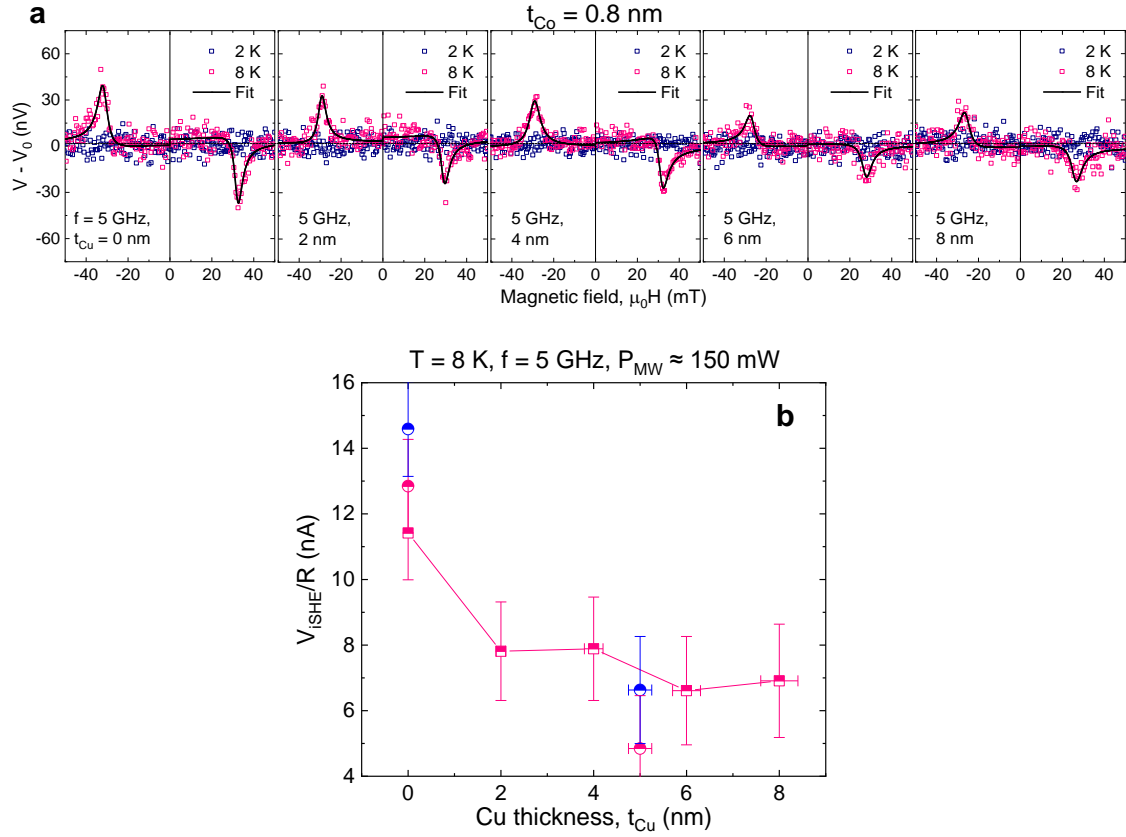


Figure S5. Reduced spin-to-charge conversion due to quenched interfacial SOC caused by Cu spacer layers. **a**, Transverse d.c. voltage measurements for asymmetric Pt(2.0 nm)/Co(0.8 nm)/Pt(1.7 nm)/Cu(t_{Cu})/Nb(30 nm)/Ni₈Fe₂(6 nm) samples with various Cu thicknesses t_{Cu} at a fixed microwave frequency $f = 5$ GHz, taken above and below the superconducting transition temperature T_c of the couple Nb. The black solid lines are fits to Lorentzian functions (see Methods). **b**, Inverse spin-Hall voltage divided by the sample's resistance V_{ISHE}/R as a function of t_{Cu} at $f = 5$ GHz.

References

- S1. Linder, J. & Robinson, J. W. A. Superconducting spintronics. *Nat. Phys.* **11**, 307–315 (2015).
- S2. Eschrig, M. Spin-polarized supercurrents for spintronics: a review of current progress.

Rep. Prog. Phys. **78**, 104501 (2015).

S3. Birge, N. O. Spin-triplet supercurrents in Josephson junctions containing strong ferromagnetic materials. *Phil. Trans. R. Soc. A* **376**, 20150150 (2018).

S4. Bergeret, F. S. & Tokatly, I. V. Spin-orbit coupling as a source of long-range triplet proximity effect in superconductor-ferromagnet hybrid structures. *Phys. Rev. B* **89**, 134517 (2014).

S5. Jacobsen, Sol H., Ouassou, Jabir A. & Linder, J. Critical temperature and tunneling spectroscopy of superconductor-ferromagnet hybrids with intrinsic Rashba-Dresselhaus spin-orbit coupling. *Phys. Rev. B* **92**, 024510 (2015).

S6. Jacobsen, Sol H., Kulagina, I. & Linder, J. Controlling superconducting spin flow with spin-flip immunity using a single homogeneous ferromagnet. *Sci. Rep.* **6**, 23926 (2016).

S7. Montiel, X. & Eschrig, M. Generation of pure superconducting spin current in magnetic heterostructures via nonlocally induced magnetism due to Landau Fermi liquid effects. *Phys. Rev. B* **98**, 104513 (2018).

S8. Amundsen, M. & Linder, J. The quasiclassical theory for interfaces with spin-orbit coupling. arXiv:1904.11986 (2019).

S9. Jeon, K.-R. et al. Enhanced spin pumping into superconductors provides evidence for superconducting pure spin currents. *Nat. Mater.* **17**, 499–503 (2018).

S10. Jeon, K.-R. et al. Exchange-field enhancement of superconducting spin pumping. *Phys. Rev. B* **99**, 024507 (2019).

S11. F. S. Bergeret, A. F. Volkov, and K. B. Efetov, *Rev. Mod. Phys.* **77**, 1321 (2005).

S12. A. I. Buzdin, *Rev. Mod. Phys.* **77**, 935 (2005).

S13. Y. V. Nazarov, *Phys. Rev. Lett.* **73**, 1420 (1994).

- S14. T. Löfwander, T. Champel, J. Durst, and M. Eschrig, *Phys. Rev. Lett.* **95**, 187003 (2005).
- S15. Bass, J. & P Pratt Jr, W. Spin-diffusion lengths in metals and alloys, and spin-flipping at metal/metal interfaces: an experimentalist's critical review. *J. Phys.: Condens. Matter* **19**, 183201 (2007).
- S16. Zhang, W., Han, W., Jiang, X., Yang, S.-H. & Parkin, S. S. P. Role of transparency of platinum–ferromagnet interfaces in determining the intrinsic magnitude of the spin Hall effect. *Nat. Phys.* **11**, 496–502 (2015).
- S17. Zhou, L. et al. Observation of spin-orbit magnetoresistance in metallic thin films on magnetic insulators. *Sci. Adv.* **4**, eaao3318 (2018).